

Detecting Dark Matter around Black Holes with Gravitational Waves: Effects of dark-matter dynamics on the gravitational waveform

Bradley J. Kavanagh,^{1,*} David A. Nichols,^{2,1,3,†} Gianfranco Bertone,^{1,‡} and Daniele Gaggero^{4,§}

¹*Gravitation Astroparticle Physics Amsterdam (GRAPPA),
Institute for Theoretical Physics Amsterdam and Delta Institute for Theoretical Physics,
University of Amsterdam, Science Park 904, 1098 XH Amsterdam, The Netherlands*

²*Department of Physics, University of Virginia, P.O. Box 400714, Charlottesville, VA 22904-4714, USA*

³*Department of Astrophysics, Faculty of Science, Radboud University
Nijmegen, P.O. Box 9010, 6500 GL Nijmegen, The Netherlands*

⁴*Instituto de Física Teórica UAM-CSIC,
Campus de Cantoblanco, E-28049 Madrid, Spain*

(Dated: January 30, 2020)

A dark matter overdensity around a black hole may significantly alter the dynamics of the black hole’s merger with another compact object. We consider here intermediate mass ratio inspirals of stellar-mass compact objects with intermediate-mass black holes “dressed” with dark matter. We first demonstrate that previous estimates based on a fixed dark-matter dress are unphysical for a range of binaries and dark-matter distributions, by showing that the total energy dissipated by the compact object through dynamical friction, as it inspirals through the dense dark matter environment towards the black hole, is larger than the gravitational binding energy of the dark-matter dress itself. We then introduce a new formalism that allows us to self-consistently follow the evolution of the dark-matter dress due to the gravitational interaction with the binary. We show that the dephasing of the gravitational waveform induced by dark matter is smaller than previously thought but still potentially detectable with the LISA space interferometer. The gravitational waves from such binaries could provide powerful diagnostics of the particle nature of dark matter.

I. INTRODUCTION

The direct detection of gravitational waves (GWs) [1–4] has opened new opportunities for fundamental physics. Present and upcoming experiments such as LIGO/Virgo [5], KAGRA [6], LISA [7, 8], Einstein Telescope [9] and Pulsar Timing Arrays [10, 11] will soon shed light on a variety of problems at the intersection between gravitational waves, black holes and fundamental physics [12], and in particular on the distribution and nature of dark matter (DM) [13, 14].

Here, we focus on the prospects for detecting and characterizing cold dark matter overdensities around black holes (BHs) using gravitational waves. If dark matter is made of cold collisionless particles, the adiabatic growth of black holes may induce the formation of large overdensities often referred to as “spikes” around supermassive [15–17] and intermediate-mass [18] astrophysical black holes, as well as around primordial black holes [19–21]. It is in principle possible to detect and characterize DM overdensities around black holes by measuring their impact on the gravitational waveform as BHs merge with other compact objects [22–30].

In this paper, we revise previous calculations of the dynamical evolution and gravitational waveforms of intermediate mass-ratio inspirals (IMRIs) around ‘dressed’

black holes, as illustrated in Fig. 1. In such a system, a stellar mass compact object (black hole or neutron star) inspirals towards an intermediate mass black hole (IMBH) with mass $10^3 - 10^5 M_\odot$. The presence of DM exerts a dynamical friction force [31–33] on the compact object, causing it to inspiral more rapidly. The resulting gravitational waveform accumulates phase at a different rate compared to the vacuum case (in the absence of DM). This ‘dephasing’ effect should be detectable with future GW observatories, but accurate waveform modeling is required to extract the signal and perform parameter estimation [34–36].

We begin by exploring energy conservation in these systems, and show that the work done by dynamical friction is typically comparable to (and in some cases much larger than) the total binding energy available in the DM spike. This means that previous calculations of the dephasing signal, which assumed a non-evolving dark matter density profile, do not conserve energy and therefore substantially over-estimate the size of the effect. In order to develop a self-consistent description of such systems, we first present N -body simulations which allow us to accurately model dynamical friction and the scattering of DM particles with the compact object. This allows us to understand where the energy lost by the compact object is injected in the DM cloud. We then devise a prescription for evolving the phase space distribution of DM as energy is ejected during the inspiral.

We self-consistently follow the evolution of the binary and the DM spike, and robustly estimate the dephasing of the gravitational waveform with respect both to vacuum inspiral, and to the unphysical case of a static DM

* b.j.kavanagh@uva.nl

† david.nichols@virginia.edu

‡ g.bertone@uva.nl

§ daniele.gaggero@uam.es

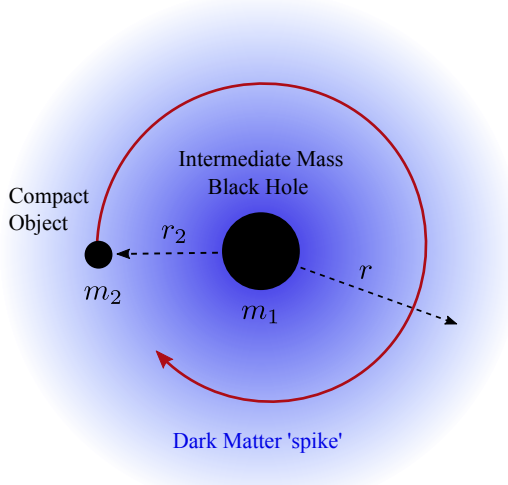


FIG. 1. **Intermediate Mass-Ratio Inspiral (IMRI) system with Dark Matter ‘spike’.** A central intermediate mass black hole (IMBH) of mass m_1 is orbited by a lighter compact object $m_2 < m_1$ at orbital radius r_2 . The IMBH is also surrounded by a ‘spike’ of Dark Matter with density profile $\rho_{\text{DM}}(r)$.

halo. We demonstrate that the dephasing of the gravitational waveform induced by dark matter is smaller than previously assumed, but still potentially detectable with the LISA space interferometer, and that it provides a powerful diagnostic of the particle nature of dark matter.

The paper is organised as follows: in Sec. II, we demonstrate that the standard approach to the dephasing signal induced by DM minispikes is likely to violate energy conservation; in Sec. III, we present N -body simulations to validate our model for dynamical friction; in Sec. IV, we present our prescription for evolving the phase space distribution of DM; in Sec. V, we use this prescription to follow the evolution of the binary and the DM spike self-consistently; finally, in Sec. VI, we discuss some caveats of this work and possible implications for the detection of such a DM spike in intermediate mass-ratio inspirals in the future.

II. ENERGY BALANCE CONSIDERATIONS WITHOUT HALO FEEDBACK

In this section, we describe the evolution of a system composed of a central IMBH with a surrounding DM spike and a lighter compact object (e.g. a neutron star) orbiting around the IMBH and through its DM cloud. This is illustrated in Fig. 1. We model the evolution of this system using Newtonian gravity, and we include dissipative effects arising from dynamical friction and gravitational radiation. Following Eda *et al.* [22, 23], we start by neglecting any feedback on the DM halo and by con-

sidering circular orbits.

A. Notation for IMBH system and DM distribution

We first define several notions of masses for the binary and the DM distribution. We will denote the mass of the IMBH by m_1 and the mass of the small compact object by m_2 . Other definitions of masses we will need are $M = m_1 + m_2$, the total mass; $q = m_2/m_1 \leq 1$, the mass ratio; $\mu = m_1 m_2 / M$, the reduced mass; and $\mathcal{M}_c = \mu^{3/5} M^{2/5}$, the chirp mass.

We assume that the IMBH is surrounded by a DM spike, formed as the adiabatic growth of the black hole enhances the central density of the host halo [16, 37–39]. The dark matter distribution will be given by

$$\rho_{\text{DM}}(r) = \begin{cases} \rho_{\text{sp}} \left(\frac{r_{\text{sp}}}{r} \right)^{\gamma_{\text{sp}}} & r_{\text{in}} \leq r \leq r_{\text{sp}} \\ 0 & r < r_{\text{in}} \end{cases}, \quad (2.1)$$

where r is the distance from the center of the IMBH. We define the inner radius of the spike to be $r_{\text{in}} = 4Gm_1/c^2$ following the results in [37]. We will not treat the DM distribution at distances $r > r_{\text{sp}}$. We also will not treat r_{sp} as a free parameter, but as determined by m_1 , ρ_{sp} and γ_{sp} via

$$r_{\text{sp}} \approx \left[\frac{(3 - \gamma_{\text{sp}}) 0.2^{3-\gamma_{\text{sp}}} m_1}{2\pi \rho_{\text{sp}}} \right]^{1/3}. \quad (2.2)$$

This assumes that $r_{\text{sp}} \approx 0.2r_h$, where r_h is defined from

$$\int_{r_{\text{in}}}^{r_h} \rho_{\text{DM}}(r) 4\pi r^2 dr = 2m_1, \quad (2.3)$$

as in [23].

We can now compute the DM mass within a distance r . The result is

$$m_{\text{enc}}(r) = \begin{cases} \frac{4\pi \rho_{\text{sp}} r_{\text{sp}}^{\gamma_{\text{sp}}}}{3 - \gamma_{\text{sp}}} (r^{3-\gamma_{\text{sp}}} - r_{\text{in}}^{3-\gamma_{\text{sp}}}) & r_{\text{in}} \leq r \leq r_{\text{sp}} \\ 0 & r < r_{\text{in}} \end{cases}. \quad (2.4)$$

It will then be convenient to define

$$m_{\text{in}} = \frac{4\pi \rho_{\text{sp}} r_{\text{sp}}^{\gamma_{\text{sp}}} r_{\text{in}}^{3-\gamma_{\text{sp}}}}{3 - \gamma_{\text{sp}}}, \quad (2.5)$$

which is the constant of integration appearing in Eq. (2.4) needed to make $m_{\text{enc}}(r)$ go to zero continuously for $r < r_{\text{in}}$. It will finally be convenient to define

$$m_{\text{DM}}(r) = m_{\text{enc}}(r) + m_{\text{in}}. \quad (2.6)$$

This is the part of $m_{\text{enc}}(r)$ without the integration constant.

With this notation set, we can now more easily discuss issues related to energy balance.

B. Gravitational potential energy of the DM distribution

To compute the total potential energy in the distribution of DM, we determine the amount of work required to assemble the distribution of DM by adding successive spherical shells of DM of increasing radius r , until the final distribution $\rho_{\text{DM}}(r)$ is constructed around the BH. We denote the potential energy of each shell of DM of radius r by $dU_{\text{sh}}(r)$. It is given by

$$dU_{\text{sh}}(r) = -\frac{G[m_1 + m_{\text{enc}}(r)]}{r} [4\pi r^2 \rho_{\text{DM}}(r) dr]. \quad (2.7)$$

After some algebra, we can instead write it as

$$dU_{\text{sh}}(r) = -\frac{G[m_1 + m_{\text{enc}}(r)]m_{\text{DM}}(r)(3 - \gamma_{\text{sp}}) dr}{r^2}. \quad (2.8)$$

Integrating Eq. (2.8) between the inner radius r_{in} and a given radius r , we arrive at the total potential energy in the distribution of DM between the radii r_{in} and r . When $\gamma_{\text{sp}} \neq 2$ or $\gamma_{\text{sp}} \neq 5/2$, the result is

$$\Delta U_{\text{DM}}(r) = -\frac{Gm_{\text{DM}}(r)(3 - \gamma_{\text{sp}})}{r} \times \left[\frac{m_1 - m_{\text{in}}}{(2 - \gamma_{\text{sp}})} + \frac{m_{\text{DM}}(r)}{5 - 2\gamma_{\text{sp}}} \right] - U_{\text{in}}, \quad (2.9)$$

where the constant U_{in} is given by

$$U_{\text{in}} = -\frac{Gm_{\text{in}}(3 - \gamma_{\text{sp}})}{r_{\text{in}}(2 - \gamma_{\text{sp}})} \left[m_1 - \frac{m_{\text{in}}(3 - \gamma_{\text{sp}})}{(5 - 2\gamma_{\text{sp}})} \right]. \quad (2.10)$$

The total potential energy of the DM spike can be obtained by evaluating Eq. (2.9) at $r = r_{\text{sp}}$. **DN: I agree with the corrected version of Eq. (2.10).**

Note that we are ignoring the gravitational potential of the small compact object on the binding energy. This will generally lead to relative errors of order q , which will be small for the systems we are considering.

C. Orbital energy and energy dissipation through GWs and DF

As a starting point, let us briefly summarize the formalism presented in Eda *et al.* [22, 23]. Since the system we are considering is characterized by a small mass ratio between the IMBH and the orbiting compact object ($q \ll 1$), we can adopt the approximation $\mu \simeq m_2$ (the errors in this approximation are of order q). This assumes that the barycenter position is equal to the IMBH position. Similarly, assuming $M = m_1$ leads to errors of order q .

Let us define the orbital energy of the orbiting object in this approximation as

$$E_{\text{orbit}} = \frac{1}{2}\mu v^2 - \frac{G(m_1 - m_{\text{in}})m_2}{r_2}, \quad (2.11)$$

where $r_2 = r_2(t)$ is the distance of the small compact object from the IMBH. We are neglecting here the contribution of the DM dress to the total energy; we have checked that it would give only a percent-level correction for the region of parameter space we are interested in. **DN: Why is m_{in} necessary if we are neglecting dark matter? Also, should clarify what parameter space is being referred to here.**

We will work with circular orbits, and we will frequently ignore the correction to the Keplerian frequency arising from the distribution of DM. In this approximation, the orbital energy reduces to the familiar expression

$$E_{\text{orbit}} = -\frac{Gm_1m_2}{2r_2}. \quad (2.12)$$

Since the light object is moving within the DM minihalo and experiencing multiple gravitational interactions with the DM particles, it loses energy via *dynamical friction* (DF) [31–33]. In addition, the orbital energy is also dissipated through the emission of gravitational waves. The timescale over which energy is radiated through these processes is slow compared to the orbital timescale for most of the evolution of the system. Thus, we will treat the dissipation as an adiabatic process slowly moving the compact object on a given circular orbit to another circular orbit with a slightly smaller radius (i.e. a quasi-circular inspiral). In this process, energy balance is satisfied, in the sense that

$$\frac{dE_{\text{orbit}}}{dt} = -\frac{dE_{\text{GW}}}{dt} - \frac{dE_{\text{DF}}}{dt}. \quad (2.13)$$

Gravitational-wave dissipation (for circular orbits in the quadrupole approximation) is given by

$$\frac{dE_{\text{GW}}}{dt} = \frac{32G^4M(m_1m_2)^2}{5(cr_2)^5}. \quad (2.14)$$

Dynamical friction losses are given by

$$\frac{dE_{\text{DF}}}{dt} = 4\pi(Gm_2)^2\rho_{\text{DM}}(r_2)\xi(v)v^{-1}\log\Lambda. \quad (2.15)$$

It will be convenient to write these losses as a function of r for circular orbits by using the relationship that $v = \sqrt{GM/r_2}$. The term $\xi(v)$ denotes the fraction of DM particles moving more slowly than the orbital speed.¹

In Eq. (2.15), $\log\Lambda$ is the usual notation for the Coulomb logarithm, defined in general as [40, App. L]:

$$\Lambda = \sqrt{\frac{b_{\text{max}}^2 + b_{90}^2}{b_{\text{min}}^2 + b_{90}^2}}, \quad (2.16)$$

¹ This term has typically been neglected in previous studies of DM dephasing [22, 23]. For the isotropic spike profile with $\gamma = 7/3$, we find $\xi(v) \approx 0.58$, independent of radius. We neglect ξ in the analytic analysis of this section, though as we will see in Sec. III, it will be necessary to include it later to obtain an accurate description of the dynamics.

where b_{\min} and b_{\max} are the minimum and maximum impact parameters for which the two-body encounters that contribute to the phenomenon can be considered effective. Moreover, b_{90} is the impact parameter which produces a 90° deflection of the DM particle:

$$b_{90} = \frac{Gm_2}{v_0^2} \approx \frac{m_2}{m_1} r_2 = q r_2, \quad (2.17)$$

with v_0 the orbital speed of the compact object. For now, we fix $\log \Lambda = 3$ (the value assumed in Eda *et al.*) although we revisit the precise value in Sec. III. **DN: I had actually been using the HaloFeedback code to compute Λ even for the static halo. It seems to be 3.45, 4.61, and 5.76 for the $q = 10^3, 10^4, 10^5$ cases.**

Using the chain rule and Eqs. (2.12), (2.14), and (2.15), we can also write an explicit expression for the time evolution of the compact object radius:

$$\dot{r}_2 = -\frac{64 G^3 M m_1 m_2}{5 c^5 (r_2)^3} - \frac{8 \pi G^{1/2} m_2 \rho_{\text{sp}} \xi \log \Lambda r_{\text{sp}}^{\gamma_{\text{sp}}}}{\sqrt{M} m_1 r_2^{\gamma_{\text{sp}} - 5/2}}. \quad (2.18)$$

As the small compact object inspirals between circular orbits with two radii r_i and r_f (with $r_i > r_f$), some fraction of the orbital energy will be carried away by GWs, and some fraction will be dissipated through dynamical friction. We write this as

$$\Delta E_{\text{orbit}} = \Delta E_{\text{DF}} + \Delta E_{\text{GW}}. \quad (2.19)$$

While the energy dissipated by GW emission is expected to have a negligible effect on the distribution of DM, the energy dissipated through DF will go directly into increasing the energy of the particles in the DM distribution.

Because the DM spike has a finite amount of potential energy, $\Delta U_{\text{DM}}(r_{\text{sp}})$, it is important to check that the energy dissipated through dynamical friction, ΔE_{DF} , is not comparable to (or in excess of) $\Delta U_{\text{DM}}(r_{\text{sp}})$. If they are comparable, then this would imply that enough energy is dissipated through DF to alter significantly the distribution of DM (and perhaps even to unbind all the DM from the gravitational potential of the IMBH). Even when the ratio $\Delta E_{\text{DF}}/\Delta U_{\text{DM}}(r_{\text{sp}})$ is comparable to but less than one, then it is generally not a good approximation that the distribution of DM would remain invariant during the inspiral of the small compact object.

Thus, it is important to compute the total energy dissipated through dynamical friction during the inspiral (i.e. compute ΔE_{DF}). This can be found by integrating Eq. (2.15) between two given times, or more conveniently, integrating the following expression between two radii, r_i and r_f describing two circular orbits:

$$\Delta E_{\text{DF}}(r_i, r_f) = - \int_{r_i}^{r_f} \frac{dE_{\text{DF}}}{dt} \left(\frac{dr_2}{dt} \right)^{-1} dr_2. \quad (2.20)$$

In Eq. (2.20), the radial evolution equation is defined in (2.18), and the energy evolution equation is defined

in (2.15). After some algebra, the integral in (2.20) can be expressed as

$$\Delta E_{\text{DF}} = -\frac{Gm_1 m_2}{2} \int_{r_i}^{r_f} \frac{dr_2}{(r_2)^2 (1 + c_r r^{-11/2 + \gamma_{\text{sp}}})}, \quad (2.21)$$

where

$$c_r = \frac{8 G^{5/2} M^{3/2} (m_1)^2}{5 \pi c^5 \rho_{\text{sp}} r_{\text{sp}}^{\gamma_{\text{sp}}} \xi \log \Lambda}. \quad (2.22)$$

The integral (2.21) can be evaluated in terms of hypergeometric functions as follows:

$$\Delta E_{\text{DF}} = \left[\frac{Gm_1 m_2}{2r_2} \times {}_2F_1 \left(1, \frac{2}{11 - 2\gamma_{\text{sp}}}, \frac{13 - 2\gamma_{\text{sp}}}{11 - 2\gamma_{\text{sp}}}; -c_r r_2^{-11/2 + \gamma_{\text{sp}}} \right) \right]_{r_f}^{r_i}. \quad (2.23)$$

This expression has an interesting form; because the hypergeometric function is a number in the range (0, 1) for positive r_2 , then (2.23) represents the difference between two fractions of the energy of two circular orbits at two radii.

Thus, with Eqs. (2.9) and (2.23), we can compute ratios of energy dissipated by dynamical friction to binding energy in the DM distribution surrounding the IMBH.

D. Ratio of energy dissipated to binding energy

In Eda *et al.*, the system investigated in greatest detail is a binary in which the IMBH has mass $m_1 = 10^3 M_\odot$ and the small compact object has mass $m_2 = 1 M_\odot$. The DM spike is characterized by a density normalization $\rho_{\text{sp}} = 226 M_\odot/\text{pc}^3$ and a power law $\gamma_{\text{sp}} = 7/3$ (the corresponding value of r_{sp} is 0.54 pc). The slope $\gamma = 7/3$ is expected to develop in the centre of a halo with an initial profile scaling as $\rho \sim r^{-1}$, such as an NFW profile [16]. Eda *et al.* observe that during the last five years as the small compact object inspirals towards the IMBH before merging, the effect of dynamical friction can significantly change the rate of inspiral. The large change in the inspiral occurs because a significant amount of energy is dissipated through dynamical friction (and thus must be balanced by increasing the kinetic energy of the DM particles in the halo).

DN: May not need this paragraph here based on updated figures. Computing the initial radius r_i such that the system merges (or, more generally reaches a second radius r_f with $r_f < r_i$) in a fixed time interval Δt is somewhat more involved when the IMBH in the binary has a surrounding distribution of DM rather than being in vacuum. We can obtain the relevant expressions needed to compute this by integrating Eq. (2.18). The result can be expressed in terms of an integral

$$\Delta t = -\frac{5c^5}{64 G^3 M m_1 m_2} \int_{r_i}^{r_f} \frac{(r_2)^3 dr_2}{1 + r_2^{11/2 - \gamma_{\text{sp}}}/c_r}, \quad (2.24)$$

or in terms of the difference of hypergeometric functions

$$\Delta t = \left[\frac{5c^5(r_2)^4}{256G^3Mm_1m_2} \times {}_2F_1 \left(1, \frac{8}{11-2\gamma_{\text{sp}}}, \frac{19-2\gamma_{\text{sp}}}{11-2\gamma_{\text{sp}}}; -r_2^{11/2-\gamma_{\text{sp}}}/c_r \right) \right]_{r_f}^{r_i}. \quad (2.25)$$

Thus, we can numerically solve Eq. (2.25) for the starting radius r_i given a time interval Δt and a radius $r_f = r_{\text{ISCO}}$, which will approximate the radius at merger.

DN: I'll properly describe the new figures soon. In the meantime, here is a crude summary: In Fig. 2, I'm defining $\Delta E_{\text{DF}}(r_2) = \Delta E_{\text{DF}}(r_2, r_{\text{ISCO}})$. The main points are that this function saturates to a constant value on the order of a few hundred gravitational radii from ISCO (dashed lines), independent of the mass ratio q , but for fixed γ_{sp} and ρ_{sp} (given by the fiducial Eda *et al.* values). For these fiducial values, having $q = 10^3$ does not satisfy this energy-balance criteria, $q = 10^4$ is borderline, and $q = 10^5$ actually seems to be okay. It also shows that it will be reasonable to use the ratio $\Delta E_{\text{DF}}(r_{\text{sp}})/\Delta U_{\text{DM}}(r_{\text{sp}})$ to assess energy balance, because this value is essentially independent of r_2 for a wide range of values of r_2 . Figure 3 then shows $E_{\text{DF}}(r_{\text{sp}})/\Delta U_{\text{DM}}(r_{\text{sp}})$ for a wide range DM parameters. It shows that energy balance is not satisfied for this wider range of DM parameter space for $q = 10^3$, there are okay and bad regions for $q = 10^4$, and that most of $q = 10^5$ is good, except for a smallish corner of the DM parameter space. This should also justify focusing our attention mostly on the $q = 10^3$ and $q = 10^4$ cases, because $q = 10^5$ would be expected to be closer to the Eda *et al.* estimates.

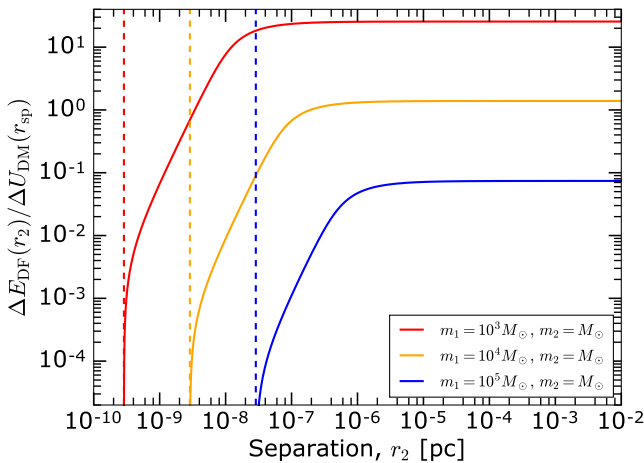


FIG. 2. **DN: TO DO**

Because $m_{\text{DM}}(r)$ satisfies the property $m_{\text{DM}}(r_{\text{sp}}) \sim m_1$, then it is not too difficult to see that the ratio $\Delta E_{\text{DF}}/\Delta U_{\text{DM}}(r_{\text{sp}})$ roughly will be proportional to q .

Thus, systems with smaller mass ratios q will generally have a smaller ratio of energy dissipated through dynamical friction to binding energy of the DM in the potential of the IMBH.

Thus, in many (though not all) of the systems considered by Eda *et al.* there is more energy dissipation through dynamical friction than binding energy in the DM distribution to account for this dissipation. It will therefore be necessary to modify the distribution of DM in response to the energy input into the DM spike through dynamical friction. Before implementing such a prescription, it would be of interest to know whether there is enough binding energy in the DM distribution to have a significant impact on the evolution of the binary. We introduce a simple effective model in Appendix A to suggest that there is indeed sufficient binding energy to have an important effect. Thus, we next turn to a more detailed description of how we implement this feedback on the DM distribution.

III. N-BODY SIMULATIONS

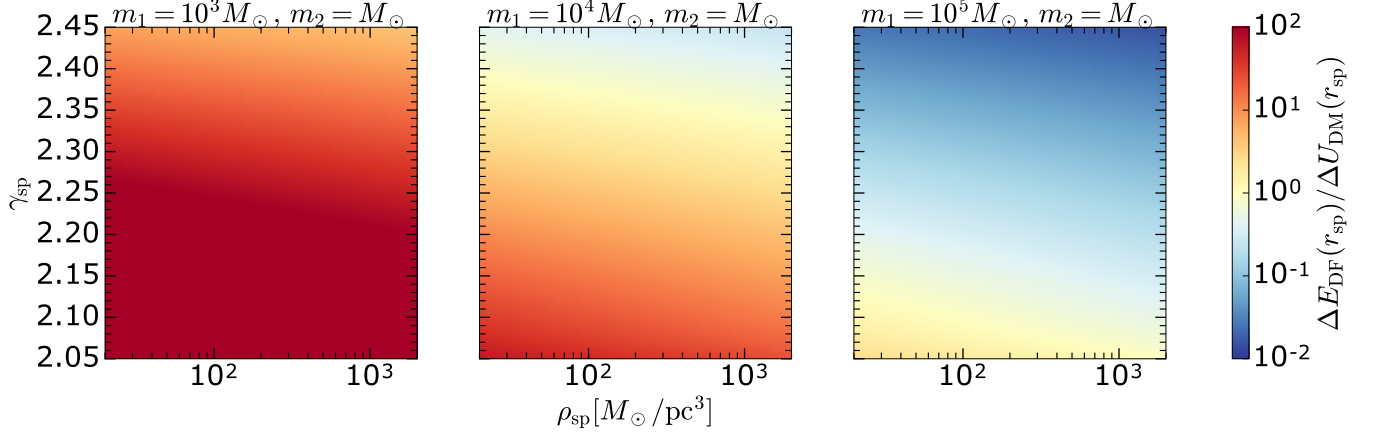
In order to build a semi-analytic prescription for feedback in the DM spike, we need to study in more detail the physics of dynamical friction in IMRI systems. In particular, as we will see in Sec. IV, we need to know the minimum and maximum impact parameter, b_{min} and b_{max} to include in our calculation of the dynamical friction effect. It is also useful to verify that the standard Chandrasekhar prescription for dynamical friction (which is derived for uniform density distributions) applies also in our setup.

For concreteness, we fix the minimum impact parameter to be $b_{\text{min}} = 10 \text{ km}$, roughly the radius of a neutron star [41]. In principle, b_{min} could be smaller (for example, if the orbiting compact object is a black hole rather than a neutron star). However, we do not need to worry about the precise value; these $\mathcal{O}(\text{km})$ scales are much smaller than any other length scales in the problem and can effectively be set to zero.

Instead, fixing the value of the maximum impact parameter b_{max} is crucial, as it determines which DM particles in the spike interact gravitationally with the orbiting compact object and therefore governs how energy is injected into the spike. Fixing b_{max} can also be seen as fixing the coulomb logarithm $\log \Lambda$, because for $b_{\text{min}} \rightarrow 0$, Eq. (2.16) becomes:

$$\log \Lambda \approx \log \left(\frac{b_{\text{max}}}{b_{90}} \right). \quad (3.1)$$

For the systems we consider here, a range of values have been previously assumed for the coulomb logarithm. Reference [29] set b_{max} equal to the orbital radius, which would be appropriate for the motion of a compact object through a diffuse host such as a galaxy [40, p.664]. For a mass ratio of $q = 10^{-4}$ and an orbital radius of

FIG. 3. **DN: TO DO**

$20Gm_1/c^2$, this gives $\log \Lambda \sim 3$, the value used by Eda *et al.* [22, 23]. For a compact object orbiting around a central point mass, we can combine Eqs. (3.1) and (2.17), to show that $\log \Lambda = \log(1/q)$ under these assumptions.

However, the dynamics of DM particles at small radii will be dominated by the central IMBH, so it seems implausible that these particles can be deflected by the smaller orbiting compact object. A more plausible approach then is to fix b_{\max} as the size of the sphere of influence of the compact object. The gravitational force from the central BH and from the compact object will be equal at a distance:

$$b_{\max} \approx \sqrt{\frac{m_2}{m_1}} r_2, \quad (3.2)$$

from the compact object. The corresponding coulomb logarithm is then:

$$\log \Lambda = \log \sqrt{\frac{1}{q}} = \log \sqrt{\frac{m_1}{m_2}}. \quad (3.3)$$

In order to determine the value of the maximum impact parameter, we perform a number of simulations using the publicly available GADGET-2 code [42, 43] as a pure N -body solver. For each simulation, we initialise a binary on a circular orbit with mass ratio $q = 10^{-3}$ - 10^{-2} , as well as a DM spike in dynamical equilibrium consisting of $N = 2^{15}$ particles. We evolve the system forward several hundred orbits and follow the evolution of the orbital separation. This allows us to calibrate the dynamical friction force and therefore determine $\log \Lambda$ and b_{\max} . In all simulations, we use as a benchmark a DM spike with $\rho_{\text{sp}} = 226 M_{\odot}/\text{pc}^3$ and a slope of $\gamma = 7/3$. Further details about the N -body simulations are given in Appendix B.

Figure 4 shows the change in orbital separation of the binary for a mass ratio $q = 10^{-2}$ and initial separation $r_2 = 3 \times 10^{-8}$ pc. Each curve shows the simulation result for a different random realisation of the DM spike. These simulations cover approximately 3 days in physical time

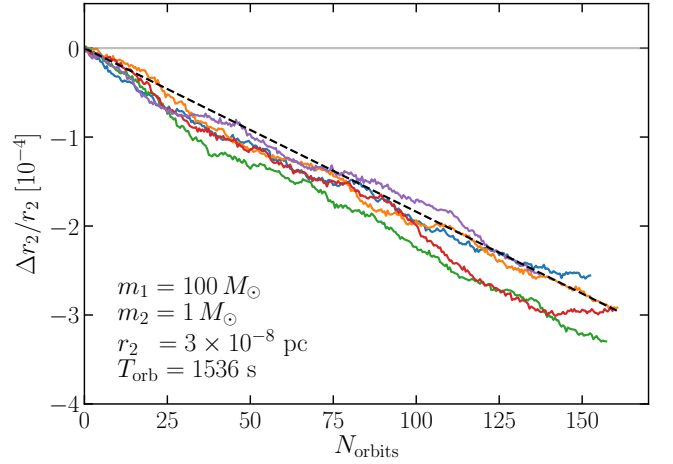


FIG. 4. **Change in binary separation.** We show the results of 5 N -body simulations which are identical except for having different initial random realisations of the DM halo. The black dashed line shows the expected change in binary separation r_2 , assuming dynamical friction losses as in Eq. (2.15) assuming $\Lambda = \sqrt{m_1/m_2}$.

and take roughly the same length of time to simulate on 16 cores. Such simulations are therefore not suitable to follow the full evolution of the binary over many years, but do allow us to measure the size of the dynamical friction losses from the change in orbital energy:

$$\frac{dE_{\text{DF}}}{dt} \approx \frac{Gm_1m_2}{2(r_2)^2} \frac{\Delta r_2}{\Delta t}. \quad (3.4)$$

For each binary configuration, we run at least 5 simulations, each for at least 100 orbits. The rate of dynamical friction energy loss in each simulation is estimated using Eq. (3.4). This allows us to estimate the mean energy loss rate, as well as the error associated with different random realisations of the DM spike.

Figure 5 shows the fractional energy loss rate due to dynamical friction for binaries with central BH mass

$m_1 = 100 M_\odot$ (top panel), $m_1 = 300 M_\odot$ (middle panel) and $m_1 = 1000 M_\odot$ (bottom panel). The dotted line in each panel shows the physical energy loss rate assuming $\log \Lambda = 1/\sqrt{q}$. For the systems we are studying, we can typically set $b_{\min} \rightarrow 0$, as discussed above. However, the simulations have a different minimum impact parameter due to their finite softening lengths l_{soft} . The dashed lines show the energy loss rate which we expect to observe in the simulations, taking into account this finite softening lengths. The data points are well fit by $b_{\min} = \frac{1}{2} l_{\text{soft}}$. As we move towards smaller separations, the maximum impact parameter shrinks, as the gravitational influence of the central BH increasingly dominates. At some point, the maximum impact parameter becomes comparable to the softening length of the simulations and the dynamical friction effect is no longer observable, shown as a sharp drop-off in the dashed curve.²

We see that in each panel of Fig. 5, the standard Chandrasekhar prescription for dynamical friction, for which we use $\Lambda = m_1/m_2$, provides a good fit to the simulations. As we increase m_1 , the uncertainties on the energy loss rate increase, as the central density of the spike grows. This in turn means that for a fixed number of DM pseudoparticles, the mass per pseudoparticle grows, giving a larger discretisation noise in the simulations. Even so, the mean dynamical friction effect estimated from the simulations matches Eq. (2.15) well. This good match requires us to include the factor $\xi \approx 0.58$, which accounts for the fraction of slow-moving DM particles and which was neglected in previous studies.

In Fig. 6, we take the data points for $r_2 = 3 \times 10^{-8}$ pc in each of the panels of Fig. 5 and plot them together. We also plot the expected size of the dynamical friction loss for different values of the coulomb term Λ . The best fit is provided by $\Lambda = \sqrt{1/q} = \sqrt{m_1/m_2}$, which was motivated by limiting the scattering to the gravitational sphere of influence of the orbiting compact object. We therefore use this value throughout the remainder of this paper, along with the corresponding value of b_{\max} :

$$b_{\max} = b_{90} \sqrt{\frac{m_1}{m_2}} = \sqrt{\frac{m_2}{m_1}} r_2. \quad (3.5)$$

We see also in Fig. 6 that the normalization of the dynamical friction loss matches that

We these results, we can also verify the standard Chandrasekhar prescription for dynamical friction, which relies on the assumption of a uniform background distribution of scattering particles. Figure 5 shows already that the dynamical friction correctly traces the DM density as a function of orbital radius, despite the fact that

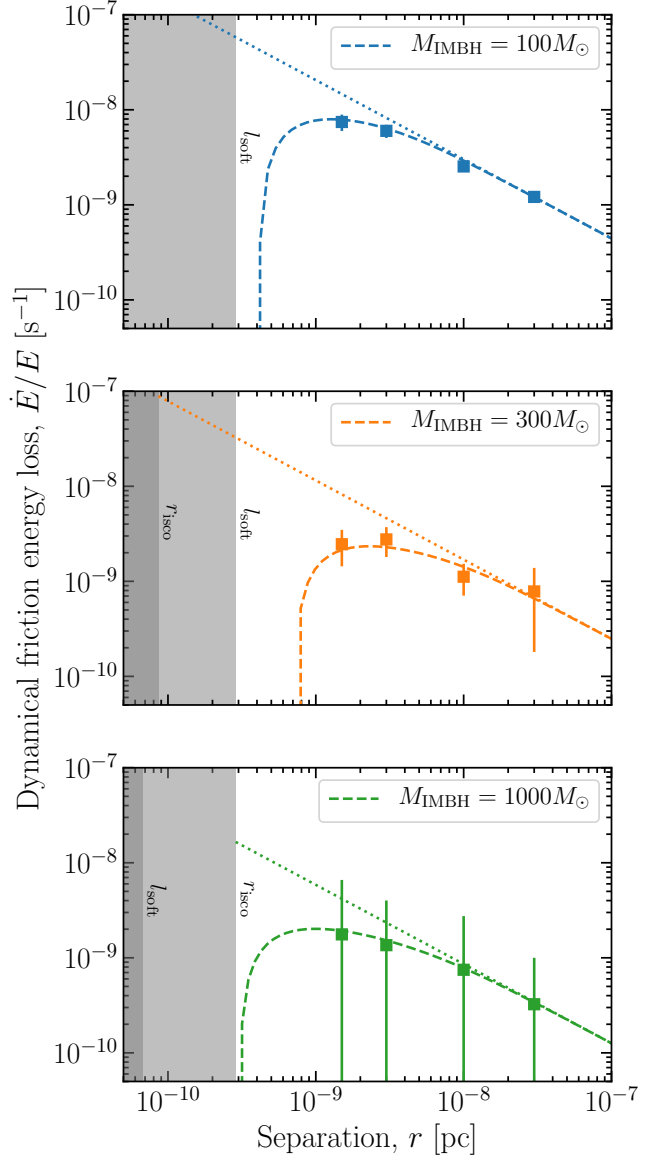


FIG. 5. **Dynamical friction energy loss estimates from N -body simulations.** The orbiting compact object has a mass $m_2 = 1 M_\odot$ and we show results for three masses of the central black hole: $100 M_\odot$ (top), $300 M_\odot$ (middle) and $1000 M_\odot$ (bottom). The diagonal dotted line shows the predicted energy loss from Eq. (2.15), assuming $\Lambda = \sqrt{m_1/m_2}$. The curved dashed line shows the energy loss accounting for the finite softening length. We also highlight in each panel the innermost stable circular orbit r_{isco} of the central IMBH, as well as the softening length l_{soft} of the simulations.

the DM distribution is not uniform. From Eq. (3.5), $b_{\max}/r_2 = \sqrt{m_2/m_1}$, meaning that for a mass ratio of $q = 10^{-3}$, b_{\max} is some 30 times smaller than the binary separation. The dynamical friction process therefore takes place only over a small region close to the orbiting compact object, meaning that the dephasing effect can be used to accurately trace out the density profile as

² Using the same logic, the maximum impact parameter is smaller for $m_1 = 1000 M_\odot$ than for the less massive central black holes. In this case of $m_1 = 1000 M_\odot$, we therefore use a slightly smaller softening length in order to preserve the dynamical friction effect down to smaller orbital separations.

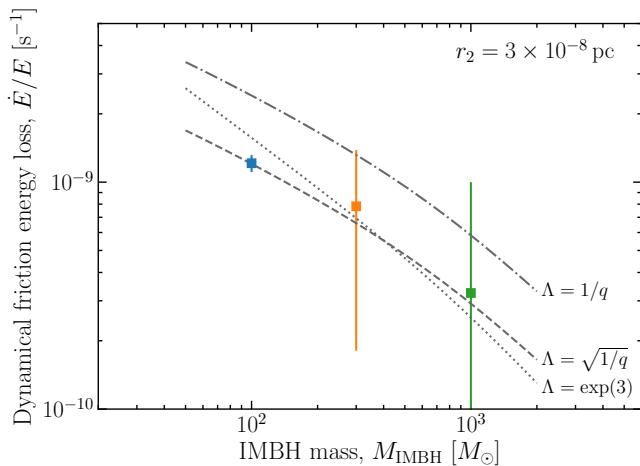


FIG. 6. **Dynamical friction energy loss as a function of IMBH mass.** The data point for each of the three masses is the same as the right-most data point in the corresponding panel of Fig. 5. Lines correspond to the predicted rates of energy loss for three different values of the coulomb factor Λ , where $q = m_2/m_1$.

a function of radius.

IV. HALO FEEDBACK

We now describe a prescription to incorporate feedback in the DM spike, which we then use in Sec. V to follow the evolution of the binary self-consistently. This prescription is semi-analytic and allows us to track the phase space distribution of the DM spike as energy is injected by the inspiraling compact object. We begin by discussing the key assumptions behind our approach.

- (a) We assume that the orbital properties evolve slowly compared to the orbital period. This assumption is justified over most of the inspiral, as discussed below Eq. (2.12), and allows us to consider the rate of energy being injected into the halo as constant over a small number of orbits.
- (b) We assume that the equilibration timescale for the DM halo is much shorter than the timescale for the secular evolution of the system. When DM particles in the halo receive a ‘kick’ from the compact object, they move to a new orbit with a larger semi-major axis. It will thus take a few orbital periods before the distribution of these particles reflects the new equilibrium density profile. However, as discussed above, the evolution of the system is slow compared to these timescales. This allows us to compute the new equilibrium density profile of the DM ‘instantaneously’ after energy is injected.
- (c) We assume that the DM halo is spherically symmetric and isotropic, and remains so throughout

the evolution of the system. This allows for a simpler treatment of the halo, as we need only keep track of the evolution of the energy of the DM particles and not their angular momentum. We discuss this assumption in more detail in Sec. VI.

With these assumptions, we can describe the DM in the spike at all times with an equilibrium phase space distribution function $f = m_{\text{DM}} dN/d^3\mathbf{r} d^3\mathbf{v}$. If the distribution of DM is spherically symmetric and isotropic, then $f = f(\mathcal{E})$ and depends only on the relative energy:

$$\mathcal{E}(r, v) = \Psi(r) - \frac{1}{2}v^2. \quad (4.1)$$

Here, $\Psi(r) = \Phi_0 - \Phi(r)$ is the relative potential, with $\Phi(r)$ the standard gravitational potential and Φ_0 a reference potential. Gravitationally bound particles then correspond to those with $\mathcal{E} > 0$. The orbital separations we are interested in lie well within the sphere of influence of the central IMBH. We therefore neglect the gravitational potential due to the DM halo and write $\Psi(r) = Gm_1/r$ (see e.g. Appendix II of Ref. [44] for a numerical comparison). This also allows us to assume that the DM halo evolves in a fixed gravitational potential, rather than having to update the potential as the DM halo is perturbed.

For a given density profile $\rho(r)$, the distribution function $f(\mathcal{E})$ can be recovered using the Eddington inversion procedure [40, p. 290]. The initial equilibrium distribution function of the spike is given by [44]:

$$f_i(\mathcal{E}) = \frac{\gamma(\gamma-1)}{(2\pi)^{3/2}} \rho_{\text{sp}} \left(\frac{r_{\text{sp}}}{Gm_1} \right)^\gamma \frac{\Gamma(\gamma-1)}{\Gamma(\gamma-\frac{1}{2})} \mathcal{E}^{\gamma-3/2}, \quad (4.2)$$

where Γ is the complete Gamma function. For a given distribution function, the density can be recovered as:

$$\rho(r) = 4\pi \int_0^{v_{\text{max}}(r)} v^2 f \left(\Psi(r) - \frac{1}{2}v^2 \right) dv, \quad (4.3)$$

where $v_{\text{max}}(r) = \sqrt{2\Psi(r)}$ is the escape velocity at radius r . Thus, if we can study the evolution of the distribution function f , we can self-consistently evolve the DM halo along with the binary and reconstruct the density profile, which is required to calculate the dynamical friction force. A similar approach to the evolution of DM BHs was applied in Refs. [18, 45].

The number of particles with energies $\mathcal{E} \rightarrow \mathcal{E} + d\mathcal{E}$ is:

$$N(\mathcal{E}) = g(\mathcal{E})f(\mathcal{E}). \quad (4.4)$$

The density of states $g(\mathcal{E})$ denotes the volume of phase space per unit energy [40, p. 292]. In the potential of the central BH, this can be calculated as:

$$\begin{aligned} g(\mathcal{E}) &= \int \delta(\mathcal{E} - \mathcal{E}(r, v)) d^3\mathbf{r} d^3\mathbf{v} \\ &= 16\pi^2 \int_0^{r_{\mathcal{E}}} dr r^2 \sqrt{2(\Psi(r) - \mathcal{E})} \\ &= \sqrt{2}\pi^3 G^3 m_1^3 \mathcal{E}^{-5/2}, \end{aligned} \quad (4.5)$$

where $r_\mathcal{E} = Gm_1/\mathcal{E}$ is the maximum radius for a particle of energy \mathcal{E} .

Let us write $P_s(\mathcal{E}, \Delta\mathcal{E})$ as the probability (over a single orbit) that a particle with energy \mathcal{E} scatters with the compact object and gains an energy $\Delta\mathcal{E}$. Then, the change in the number of particles at energy \mathcal{E} over a single orbit can be written as:

$$\begin{aligned} \Delta N(\mathcal{E}) = & -N(\mathcal{E}) \int P_s(\mathcal{E}, \Delta\mathcal{E}) d\Delta\mathcal{E} \\ & + \int N(\mathcal{E} - \Delta\mathcal{E}) P_s(\mathcal{E} - \Delta\mathcal{E}, \Delta\mathcal{E}) d\Delta\mathcal{E}, \end{aligned} \quad (4.6)$$

where the integration is over the range $[\Delta\mathcal{E}(b_{\max}), \Delta\mathcal{E}(b_{\min})]$. The first term in Eq. (4.6) describes those particles initially at energy \mathcal{E} which scatter to another energy, while the second term corresponds to those particles which scatter from energies $\mathcal{E} - \Delta\mathcal{E}$ to energy \mathcal{E} .

We will describe the evolution of the system in terms of the distribution function $f(\mathcal{E}) = N(\mathcal{E})/g(\mathcal{E})$. Assuming that the evolution of the system is much slower than the orbital frequency, we can write $\Delta f \approx T_{\text{orb}} df/dt$, with $T_{\text{orb}} = 2\pi\sqrt{(r_2)^3/(GM)}$ the orbital period. Thus, we obtain:

$$\begin{aligned} T_{\text{orb}} \frac{df(\mathcal{E})}{dt} = & -f(\mathcal{E}) P_s(\mathcal{E}) + \\ & \int \left(\frac{\mathcal{E}}{\mathcal{E} - \Delta\mathcal{E}} \right)^{5/2} f(\mathcal{E} - \Delta\mathcal{E}) P_s(\mathcal{E} - \Delta\mathcal{E}, \Delta\mathcal{E}) d\Delta\mathcal{E}, \end{aligned} \quad (4.7)$$

where $P_s(\mathcal{E}) = \int P_s(\mathcal{E}, \Delta\mathcal{E}) d\Delta\mathcal{E}$ is the total probability for a particle of energy \mathcal{E} to scatter with the compact object during one orbit. Using Eq. (4.7), we can evolve the distribution function over a number of orbits (assuming that the binary separation changes slowly compared to the orbital period). The density profile throughout the spike can then be derived using Eq. (4.3), which in turn is used to evaluate the rate of energy loss due to dynamical friction, given in Eq. (2.15).

The final step is then to evaluate $P_s(\mathcal{E}, \Delta\mathcal{E})$. When a DM particle passes the compact object with impact parameter b , it is deflected and the velocity of the compact object parallel to its motion changes.³ The change in speed of the compact object is [40, App. L]:

$$\Delta v_{\parallel} = -2v_0 \frac{m_{\text{DM}}}{m_2} \left[1 + \frac{b^2}{b_{90}^2} \right]^{-1}, \quad (4.8)$$

where v_0 is the relative speed of the encounter, which we take to be of order the orbital speed, and b_{90} was defined

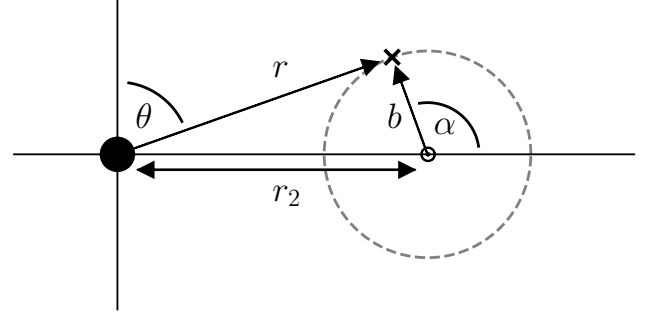


FIG. 7. **Geometry of DM scattering around the compact object.** The compact object position is denoted \odot , at a radius r_2 from the central IMBH. The motion of the compact object is into (or out of) the page. See Eqs. (4.12)-(4.16) for more details.

in Eq. (2.17). The change in energy of the compact object is then

$$\Delta E = \frac{1}{2} m_2 [(v_0 + \Delta v_{\parallel})^2 - v_0^2] \approx m_2 v_0 \Delta v_{\parallel}, \quad (4.9)$$

meaning that by energy conservation the change in relative energy \mathcal{E} of a single DM particle is:

$$\Delta\mathcal{E}(b) = -\frac{\Delta E}{m_{\text{DM}}} = -2v_0^2 \left[1 + \frac{b^2}{b_{90}^2} \right]^{-1}. \quad (4.10)$$

We assume that only DM particles with speeds slower than $v_0 \sim v_{\text{orb}}$ will scatter and gain energy from the orbiting compact object [31]. Particles moving faster than v_0 will instead give rise to dynamical heating, increasing the energy of the compact object. However, this effect is suppressed by the ratio m_2/m_{DM} and can safely be neglected in this scenario [40, p. 582].

The scattering probability can now be evaluated as:

$$\begin{aligned} P_s(\mathcal{E}, \Delta\mathcal{E}) = & \frac{1}{g(\mathcal{E})} \iint_{r < r_\mathcal{E}, v < v_0} \delta(\mathcal{E}(r, v) - \mathcal{E}) \\ & \times \delta(\Delta\mathcal{E}(b) - \Delta\mathcal{E}) d^3\mathbf{r} d^3\mathbf{v}. \end{aligned} \quad (4.11)$$

Evaluating the integral over \mathbf{v} , as in Eq. (4.5), and using Eq. (4.10) to change the argument of the second δ -function, we obtain:

$$\begin{aligned} P_s(\mathcal{E}, \Delta\mathcal{E}) = & \frac{\pi b_{90}^2}{g(\mathcal{E}) v_0^2} \int_{r_{\text{cut}}}^{r_\mathcal{E}} \frac{1}{b} \left[1 + \frac{b^2}{b_{90}^2} \right]^2 \\ & \times \delta(b - b_\star(\Delta\mathcal{E})) \sqrt{2(\Psi(r) - \mathcal{E})} d^3\mathbf{r}. \end{aligned} \quad (4.12)$$

Here, we have defined $b_\star = b_{90} \sqrt{2v_0^2/|\Delta\mathcal{E}| - 1}$ and the lower limit $r_{\text{cut}} = Gm_1/(\mathcal{E} + \frac{1}{2}v_0^2)$ ensures that only particles with $v < v_0$ can scatter with the orbiting compact object.

³ Note that we don't consider changes in the velocity *perpendicular* to the motion of the compact object because on average these do not give rise to a change in energy.

Equation (4.12) now involves an integral over the entire DM spike, with a contribution only from positions with impact parameters $b = b_*(\Delta\mathcal{E})$. This corresponds to an integral over the torus with minor radius $b_*(\Delta\mathcal{E})$ and major radius r_2 , the orbital radius of the compact object. For $b \ll r_2$, we can perform the azimuthal integral over the orbit:

$$\int r^2 dr d\cos\theta d\phi \rightarrow 2\pi r_2 \int \sin\theta r dr d\theta, \quad (4.13)$$

where (r, θ, ϕ) are the standard spherical polar coordinates. Finally, we change variables from (r, θ) to (b, α) , where the angle $\alpha \in [0, 2\pi]$ is defined as in Fig. 7. With this, we have:

$$\int \sin\theta r dr d\theta \rightarrow 2 \int_0^\pi \int_0^\infty \sin(\theta[b, \alpha]) b db d\alpha. \quad (4.14)$$

Substituting in Eq. (4.12) and performing the integral over b , we finally obtain:

$$P_s(\mathcal{E}, \Delta\mathcal{E}) = \frac{4\pi^2 r_2 b_{90}^2}{g(\mathcal{E}) v_0^2} \left[1 + \frac{b_*^2}{b_{90}^2} \right]^2 \times \int \sqrt{2(\Psi(r[b_*, \alpha]) - \mathcal{E})} \sin(\theta[b_*, \alpha]) d\alpha. \quad (4.15)$$

The radial coordinate r is now expressed as:

$$r[b_*, \alpha] = [r_2^2 + b_*^2 + 2r_2 b_* \cos\alpha]^{1/2}, \quad (4.16)$$

and we integrate over all values of $\alpha \in [0, \pi]$ such that $r[b_*, \alpha] \in [r_{\text{cut}}, r_{\mathcal{E}}]$. We work to first order in b_*/r_2 , in which case Eq. (4.15) can be written in terms of elliptic integrals; more details are provided in Appendix C. Code for computing the properties and time evolution of the DM spike is publicly available online at <https://github.com/bradkav/HaloFeedback> [?].

A. Testing the halo feedback

Before tackling the complete IMRI system including a dynamic DM spike, we first test the formalism by following the evolution of the DM distribution in a simpler scenario. We consider a mass $m_2 = 1 M_\odot$ orbiting a central BH $m_1 = 1000 M_\odot$ at a distance $r_2 = 10^{-8}$ pc. This configuration is a typical snapshot of an IMRI signal which would be observable by LISA, except that we will keep the orbital separation *fixed*. That is, we will look only at how the DM spike evolves in response to energy injection, without allowing the orbit of the compact object to change.

Figure 8 shows the result of this ‘test’ simulation, run over 40000 orbits. We plot the density profile of the spike, including only those particles moving more slowly than the local orbital speed $v < v_{\text{orb}}(r)$ (i.e. only those particles which would produce a net dynamical friction effect

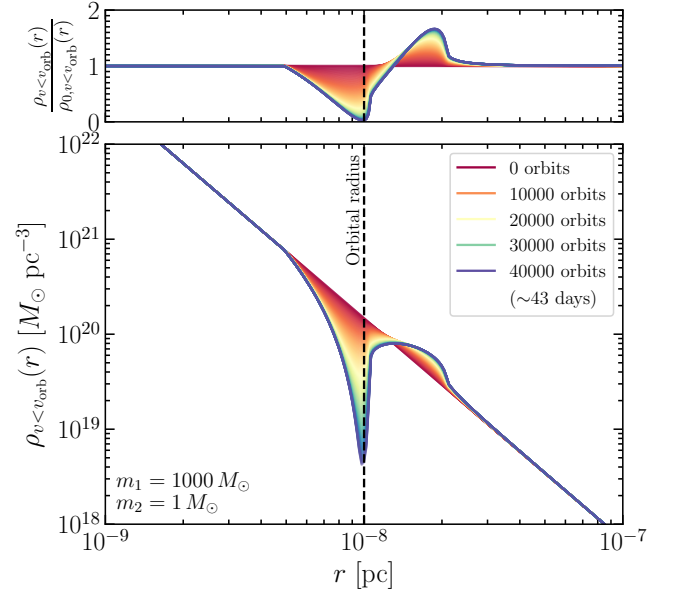


FIG. 8. **Evolution of the DM spike density profile due to feedback from the orbiting object.** We consider an compact object $m_2 = 1 M_\odot$ orbiting at a *fixed* radius $r = 10^{-8}$ pc from the IMBH with $m_1 = 1000 M_\odot$. Note that we plot $\rho_{\text{DM}}(r)$ multiplied by the fraction of DM at radius r moving more slowly than the local orbital speed $v_{\text{orb}}(r)$. The upper panel shows the evolution of the density profile normalised to the density profile ρ_0 at the start of the simulation.

on the orbiting compact object). DM particles are gradually depleted from close to the compact object through scattering; at the end of the simulation, the density at the orbital radius has dropped to 3% of the initial density. We note that particles with some energy \mathcal{E} naturally populate radii between $r = 0$ and $r = r_{\mathcal{E}} = Gm_1/\mathcal{E}$. This means that particles scattering at a radius r_2 will also deplete particles at smaller radii, as observed in Fig. 8. These scattered particles gain energy and their average radius increases, leading to a bump in the density profile at $r > r_2$.

By comparing the change in energy of the DM spike and the work which would be done on the compact object by dynamical friction, we have confirmed that energy is conserved at the level of 1%, with approximately 6% of the total energy carried away by particles which become completely unbound from the spike. Unlike in the case of a static DM spike, this feedback formalism allows us to follow the system self-consistently, ensuring that energy is conserved throughout its evolution.

V. EVOLUTION OF THE BINARY WITH HALO FEEDBACK

In this section, we incorporate the halo feedback prescription in Sec. IV into our evolution of the binary system. In Sec. II, we could determine the dynamics of the binary from solving a single, ordinary differential equation for the orbital separation of the binary, Eq. (2.18), in a static distribution of dark matter, Eq. (2.1). In this section, we instead simultaneously evolve the orbital separation of the binary in a spherically symmetric distribution of dark matter, which itself evolves in response to the inspiral of the small compact object from dynamical friction. Thus, the evolution equation for \dot{r}_2 has a similar form to that in Eq. (2.18), but we replace $\rho_{\text{DM}}(r)$ with the time-dependent DM distribution, which we denote $\rho_{\text{DM}}(r, t; r_2)$. Similarly, the fraction of DM particles slower than the circular speed at r_2 is written $\xi(r, t; r_2)$. The expression, in full, is

$$\dot{r}_2 = - \frac{64 G^3 M m_1 m_2}{5 c^5 (r_2)^3} - \frac{8 \pi G^{1/2} m_2 \log \Lambda r_2^{5/2} \rho_{\text{DM}}(r, t; r_2) \xi(r, t; r_2)}{\sqrt{M} m_1}. \quad (5.1)$$

Because the evolution of $\rho_{\text{DM}}(r, t; r_2) \xi(r, t; r_2)$ depends upon r_2 we must simultaneously evolve Eq. (5.1) with the prescription in Sec. IV for evolving the dark matter distribution.

There are two types of subtleties that arise when evolving the binary with the halo feedback, which are related to (i) initial conditions and (ii) the size of the time steps used to evolve the system. We discuss each of these issues now in more detail.

(i) Regarding initial conditions, for simplicity, one would like to be able to use the static DM distribution, Eq. (2.1), as the initial condition for evolving the binary with halo feedback. However, unless the small compact object suddenly materialized in its orbit, this will generally not be a realistic initial condition. Rather, one would expect that the small compact object was either captured, or it formed at a larger radius, and altered the dark matter distribution via feedback on the halo until it reaches an orbital separation from where it will merge within a few years. This could make simulating the binary challenging, because the exact initial conditions could depend upon the history of how the binary formed.

However, as we saw in Sec. III, the particles that contribute to this gravitational drag force lie within some small range of impact parameters from the compact object. One might anticipate then that outside of some distance from the small compact object, the distribution of dark matter is not strongly affected, and the static distribution of dark matter, Eq. (2.1), remains a good approximation for the density within this region. If we are interested in evolving the binary using more realis-

tic initial conditions for an initial separation r_i , then we would need to start evolving the system from a larger separation $r_i + \Delta r_i$, where we have defined Δr_i to be the distance outside of which the distribution of dark matter is not significantly affected by the gravitational scatterings that produce dynamical friction. We will take this approach described here to set what we believe to be reasonable initial conditions for the evolution of the binary and the dark-matter spike; in practice, we set $\Delta r_i = 2r_i$.

(ii) Regarding the size of time steps, we note that the method of Sec. IV for evolving the dark-matter halo is only valid over timescales of (at least) a few orbital periods. Thus, we will be limited in the size of the time steps that we can take to be this size or greater. While this will not be problematic when the system is adiabatically evolving between circular orbits, our errors could be large when the binary is more relativistic, and the orbital radius changes more rapidly. Ultimately, we do not view this as a large problem, because the Newtonian approximation that we adopt throughout this paper runs into other inaccuracies when the system is sufficiently relativistic that we would like to be taking a smaller time step. We discuss these issues in more details in Sec. VI. Nevertheless, because we can only take timesteps that are an integral number of the orbital period, we will not be able to resolve the orbital phase (or changes in phase) to less than integral multiples of 2π (i.e., less than one orbit).

We will focus on our fiducial spike with $\rho_{\text{sp}} = 226 M_\odot/\text{pc}^3$ slope $\gamma = 7/3$, though we also present results for shallower slopes. By comparing our numerical integration with the analytic calculation in the case of the vacuum inspiral, we find that our results have an absolute error of approximately $\mathcal{O}(50)$ cycles over the entire inspiral.

As we saw in Sec. IV A, feedback on the DM halo leads to a depletion of the DM density at the orbital radius. This in turn reduces the size of the dynamical friction force and thus slows the inspiral. There is therefore competition between how quickly the compact object depletes DM and how rapidly dynamical friction causes it to lose energy. If the inspiral is sufficiently fast, the compact object moves to an orbit at smaller radius before all of the DM is depleted and the overall effect of feedback will be relatively small. Instead, if the inspiral is slow, most of the DM will be depleted at the current orbital radius and the binary will effectively stall. At this stage GW energy losses dominate and the binary must move slowly to a smaller radius before dynamical friction can dominate again. In this case, the behaviour of the system is significantly altered by feedback. Animations showing the co-evolution of the binary and DM profile are available online at [?]. **BJK: Some of the following text/plots need to be re-arranged to improve the flow.**

DN: Table II is just a temporary addition. The main point is that it shows that different conventions for computing what “dephasing” means can

TABLE I. **Change in the number of cycles during the inspiral.** Change in the total number of GW cycles (compared with a 5-year vacuum inspiral) due to dynamical friction. **BJK: Clarify how we fix the initial frequency?** We compare results for a static DM halo and a dynamic DM halo incorporating feedback. In the top and bottom tables, we show results for mass ratios of $q = 10^{-3}$ and $q = 10^{-4}$ respectively. We also indicate the number of cycles expected in vacuum (in the absence of DM). **DN: Reformatted a bit to conform with PRD table styles. NOTE: PRD does not allow vertical lines in tables, so we may want to reformat where we put ΔN_{cycles} for clarity BJK: I've updated these numbers to reflect method (ii) for calculating ΔN .**

$m_1 = 10^3 M_\odot, N_{\text{cycles}} = 5.71 \times 10^6$ in vacuum				
ΔN_{cycles}	$\gamma = 1.5$	$\gamma = 2.2$	$\gamma = 2.3$	$\gamma = 2.33$
Static	< 1	2.4×10^4	1.6×10^5	2.8×10^5
Dynamic	< 1	1.3×10^2	8.8×10^2	1.7×10^3

$m_1 = 10^4 M_\odot, N_{\text{cycles}} = 3.20 \times 10^6$ in vacuum				
ΔN_{cycles}	$\gamma = 1.5$	$\gamma = 2.2$	$\gamma = 2.3$	$\gamma = 2.33$
Static	< 1	1.4×10^3	8.7×10^3	1.6×10^4
Dynamic	< 1	1.6×10^2	1.0×10^3	1.9×10^3

$m_1 = 10^5 M_\odot, N_{\text{cycles}} = 1.7 \times 10^6$ in vacuum				
ΔN_{cycles}	$\gamma = 1.5$	$\gamma = 2.2$	$\gamma = 2.3$	$\gamma = 2.33$
Static	< 1	7.7×10^1	4.5×10^2	8.2×10^2
Dynamic	< 1	4.6×10^1	2.8×10^2	5.1×10^2

lead to dephasing estimates that differ by almost an order of magnitude. The four conventions are as follows: (i) “ f_{vac} set— t_{DM} varies”, setting the initial frequency for the DM inspiral based on the value for a 5-year inspiral to merger in vacuum, so that DM mergers take place in less time; (ii) “ t_{vac} set— f_{DM} varies”, fixing the time to merger to be 5 years for both vacuum and DM inspirals so that DM mergers must start at lower frequencies; (iii) “ f_{DM} set— t_{vac} varies”, using the initial frequency based on the DM value for a 5-year DM inspiral to merger for both vacuum and DM inspirals, so that vacuum inspirals take more time to merger; and (iv) “ t_{DM} set— f_{vac} varies”, again setting the frequency for a 5-year time to merger for the DM system, but now the vacuum inspiral stops at a frequency $f_{\text{vac},f}$ after 5 years, before merging. The bottom two tables show (above)

the starting frequencies such that the system with DM will merge in 5 years, and (below) the final frequencies that the vacuum system will reach after inspiraling for 5 years from the frequencies in the table above. (I can also compute the differences in the times from 5 years for the other two cases if it would be helpful.)

TABLE II. **DN: Analytical calculations of “dephasing” from a static halo for four ways of computing the dephasing (see text for descriptions).**

$m_1 = 10^3 M_\odot, N_{\text{cycles}} = 5.71 \times 10^6$ in vacuum					
Set	Vary	$\gamma = 1.5$	$\gamma = 2.2$	$\gamma = 2.3$	$\gamma = 7/3$
f_{vac}	t_{DM}	< 1	1.2×10^5	6.4×10^5	1.0×10^6
t_{vac}	f_{DM}	< 1	2.5×10^4	1.6×10^5	2.9×10^5
f_{DM}	t_{vac}	~ 1	2.2×10^5	1.3×10^6	2.3×10^6
t_{DM}	f_{vac}	-5.1×10^1	-4.9×10^5	-1.2×10^6	-1.5×10^6

$m_1 = 10^4 M_\odot, N_{\text{cycles}} = 3.20 \times 10^6$ in vacuum					
Set	Vary	$\gamma = 1.5$	$\gamma = 2.2$	$\gamma = 2.3$	$\gamma = 7/3$
f_{vac}	t_{DM}	< 1	7.1×10^3	4.2×10^4	7.4×10^4
t_{vac}	f_{DM}	< 1	1.5×10^3	8.8×10^3	1.6×10^4
f_{DM}	t_{vac}	< 1	1.3×10^4	7.5×10^4	1.4×10^5
t_{DM}	f_{vac}	-1.4	-6.7×10^4	-2.0×10^5	-2.8×10^5

$m_1 = 10^3 M_\odot, f_{\text{GW}} = 2.26 \times 10^{-2} \text{Hz}$ in vacuum					
$m_1 = 10^4 M_\odot, f_{\text{GW}} = 1.27 \times 10^{-2} \text{Hz}$ in vacuum					
Mass	$\gamma = 1.5$	$\gamma = 2.2$	$\gamma = 2.3$	$\gamma = 7/3$	
$10^3 M_\odot$	2.26×10^{-2}	2.24×10^{-2}	2.12×10^{-2}	2.01×10^{-2}	
$10^4 M_\odot$	1.27×10^{-2}	1.27×10^{-2}	1.26×10^{-2}	1.26×10^{-2}	

Mass	$\gamma = 1.5$	$\gamma = 2.2$	$\gamma = 2.3$	$\gamma = 7/3$	
$10^3 M_\odot$	4.25×10^0	8.65×10^{-2}	4.24×10^{-2}	3.29×10^{-2}	
$10^4 M_\odot$	4.40×10^{-1}	1.14×10^{-1}	5.88×10^{-2}	4.70×10^{-2}	

DN: I think (i) and (iii) make more sense for a detector like LIGO, where sources enter into band at a fixed frequency, and the amount of dephasing changes the amount of time that a signal is in band. (This is also related to the fact that signals that are in band for less than five years will be less

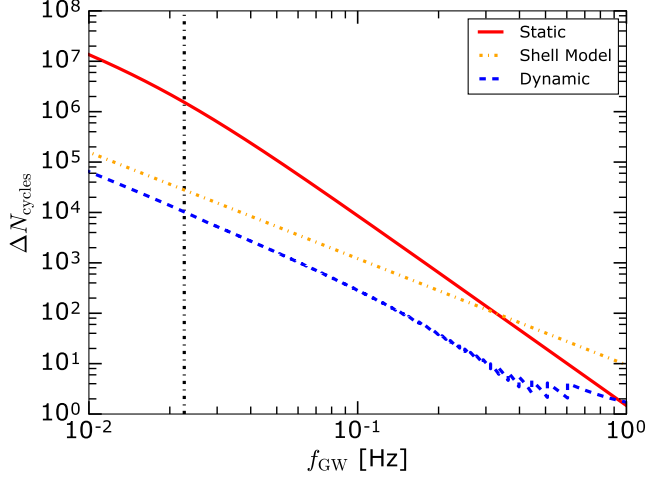


FIG. 9. Change in the number of GW cycles with respect to the vacuum inspiral. **DN: This is a temporary (but improved) version. There are still some bugs to be worked out. Will hopefully update soon.** For a mass ratio $q = 10^{-3}$, we show the change in the number of cycles (compared to the case without DM) starting from GW frequency f up to the merger.

prevalent, and may be harder to detect.) I think (ii) and (iv) make more sense for LISA, where the sources are likely to be in band for the full duration of the operation of the satellites, so the dephasing is with respect to the number of cycles anticipated during the detector operation time. We can discuss this point more if helpful.

DN: Here are some definitions and formulas I use for computing the number of cycles. This might not be the best placement for “readability” of the text.

We define the number of GW cycles by integrating the GW frequency as a function of time between two times,

$$N_{\text{cycles}}(t_f, t_i) = \int_{t_i}^{t_f} f_{\text{GW}}(t) dt. \quad (5.2)$$

In the quadrupole approximation, the GW frequency f_{GW} is twice the orbital frequency $\Omega_{\text{orb}}(t)/(2\pi)$. Combining this with the leading Newtonian expression for the evolution of the frequency allows the number of GW cycles to be computed in vacuum through the expression

$$N_{\text{cycles}}^{\text{vac}}(f_{\text{GW},f}, f_{\text{GW},i}) = \frac{1}{\pi} \left(\frac{8\pi G M_c f}{c^3} \right)^{-5/3} \bigg|_{f_{\text{GW},i}}^{f_{\text{GW},f}}. \quad (5.3)$$

In the presence of a static dark-matter distribution, it is

possible to show that

$$N_{\text{cycles}}^{\text{DM}}(f_{\text{GW},f}, f_{\text{GW},i}) = \left[\frac{1}{\pi} \left(\frac{8\pi G M_c f}{c^3} \right)^{-5/3} \times {}_2F_1 \left(1, \frac{5}{11-2\gamma_{\text{sp}}}, \frac{16-2\gamma_{\text{sp}}}{11-2\gamma_{\text{sp}}}; -c_f f^{-11/3+2\gamma_{\text{sp}}/3} \right) \right] \bigg|_{f_{\text{GW},i}}^{f_{\text{GW},f}}. \quad (5.4)$$

The coefficient c_f is defined by

$$c_f = \frac{5Gc^5 q \rho_{\text{sp}} r_{\text{sp}}^{\gamma_{\text{sp}}} \log \Lambda}{(G M_c)^{5/3} (G M)^{\gamma_{\text{sp}}/3} \pi^{(8-2\gamma_{\text{sp}})/3}} \quad (5.5)$$

We define the difference in cycles between inspirals with and without dark matter by

$$\Delta N_{\text{cycles}} = N_{\text{cycles}}^{\text{vac}}(f_{\text{GW},f}, f_{\text{GW},i}) - N_{\text{cycles}}^{\text{DM}}(f_{\text{GW},f}, f_{\text{GW},i}) \quad (5.6)$$

DN: For some choice of frequencies or elapsed times, which will be settled on later...

In order to quantify the size of the dephasing effect, we estimate the difference between the number of gravitational wave cycles N_{cycles} during the inspiral in vacuum and in presence of the DM mini-spike, for both the dynamic and static case. These values are listed in Table I. Having in mind a 5 year observation with LISA, we measure ΔN_{cycles} starting from a separation such that the time-to-merger is 5 years in the vacuum case. For a $10^3 M_{\odot}$ ($10^4 M_{\odot}$) IMBH, this corresponds to an initial separation of $r_2 = 9.638 \times 10^{-9}$ pc ($r_2 = 3.048 \times 10^{-8}$ pc). Dynamical friction has the effect of speeding up the inspiral, reducing the number of GW cycles which would be observed by experiments such as LISA.

For a central IMBH with $m_1 = 10^3 M_{\odot}$, assuming a static DM spike with slope $\gamma = 7/3$, the dephasing effect would reduce the number of GW cycles by roughly 18%. However, modelling also the dynamics of the spike, which responds to feedback from the orbiting compact object, the dephasing effect is reduced to 0.2%. As we saw in Fig. ??, previous calculations assuming a ‘static’ DM spike overestimated the amount of energy available by an order of magnitude. Here, we see that incorporating DM feedback is not a small correction, but instead reduces the size of the dephasing effect by roughly an order of 50.

For a heavier central IMBH of $m_2 = 10^4 M_{\odot}$, the binding energy available in the DM spike is larger. As shown in Fig. ??, this available energy is at least an order of magnitude larger than the work done by dynamical friction. This is reflected in the smaller difference between the results for ‘static’ and ‘dynamic’ spikes. The dephasing would appear as a roughly 2% effect if we assumed a ‘static’ spike. Note that the size of the effect is smaller for a heavier IMBH because dynamical friction is subdominant to GW energy losses (for the initial separation we consider here). The dephasing effect is reduced by 60% once we incorporate dynamic feedback of the DM.

For a spike with slope $\gamma = 7/3$, dephasing effect still corresponds to a difference of 29000 GW cycles, which should be observable and distinguishable by LISA **BJK: citation? quantification?**

The difference between N_{cycles} in vacuum and in presence of DM, as a function of the initial frequency, is also visualized in Fig. 9. In this figure we compare the ‘static’ (blue line) and ‘dynamic’ (red line) cases, and also consider a ‘shell’ evolution characterized by...

BJK: Need to be consistent with γ vs γ_{sp} throughout...

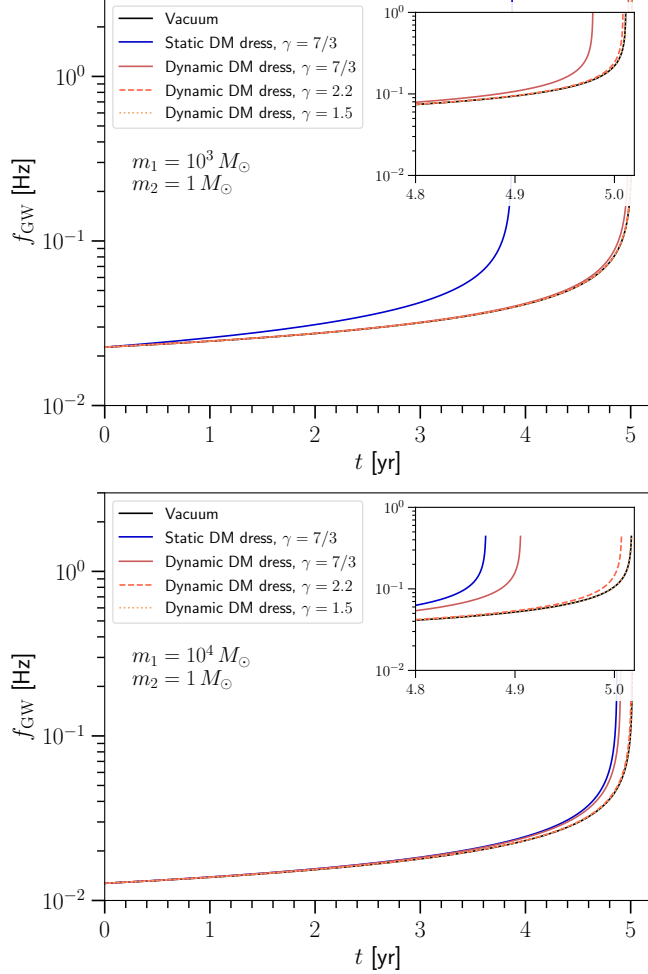


FIG. 10. **Frequency evolution of the IMRI system.** Gravitational wave frequency of the binary as a function of time, starting approximately 5 years before the merger. The black curve shows the evolution in the absence of a DM spike, while the colored curves show the evolution for spikes with characteristic density $\rho_{\text{sp}} = 226 M_{\odot}/\text{pc}^3$ and different slopes γ . **Top:** mass ratio $q = 10^{-3}$. **Bottom:** mass ratio $q = 10^{-4}$.

As well as reducing the number of GW cycles, dynamical friction is also expected to shorten the inspiral time [28] and change the density profile of the DM mini-spike.

In Fig. 10, we plot spectrograms, showing the frequency evolution of the GW signal with time. For a mass

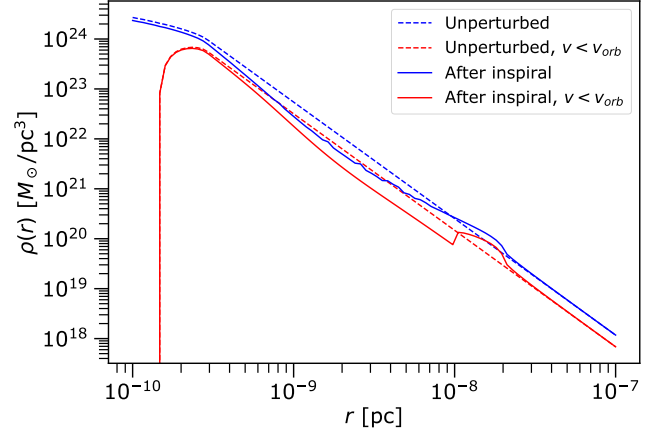


FIG. 11. **Evolution of the DM mini-spike profile.** The solid lines refer to the system at the end of the inspiral, while the dashed lines correspond to the initial, unperturbed configuration. Blue lines: total density profile. Red lines: density profiles associated to the particles slower than the circular speed $v_{\text{orb}}(r)$ for each r .

ratio $q = 10^3$, the assumption of a static DM spike implies that a 5-year inspiral in vacuum would be shortened by more than 1 year in the presence of a DM spike with $\gamma = 7/3$. However, our self-consistent model substantially reduces the size of the effect, leading to an inspiral which is just 12 days shorter than the vacuum case. We also see that the dephasing effect is very sensitive to the slope of the DM distribution, rapidly becoming undetectable for a mild slope of $\gamma = 3/2$.

In Fig. 11 we show the effect of the inspiral on the density profile of the DM mini-spike. We notice that, after the inspiral, the DM density at each radius is altered at most by a factor of 2 with respect to the initial configuration.

BJK: Need to talk about Fig. 9 and discuss the ‘shell’ estimate for the dephasing.

BJK: Do we need to talk about what the profile looks like at the end? How much is it disrupted?

DG: Added a plot on that

VI. DISCUSSION

In this section, we discuss a number of caveats to the calculations we have performed. We suggest a number of avenues for improvements in the future as well as the prospects for detecting the dephasing signal.

A. Halo relaxation

Thus far, we have assumed that the DM halo is disrupted by the orbiting compact object and does not evolve further. We now consider processes which may *replenish* the depleted halo. One possibility is that DM

particles may diffuse in energy through small-angle scattering with each other, ultimately refilling the depleted regions. Following Refs. [46, 47], the relaxation time associated with this process scales as

$$t_{\text{relax}} \sim \frac{\sigma_v^3}{G^2 m_{\text{DM}}^2 n_{\text{DM}}} \approx \frac{m_1^{3/2}}{G^{1/2} \rho_{\text{DM}} m_{\text{DM}} r^{3/2}}, \quad (6.1)$$

where the DM velocity dispersion is approximately $\sigma_v^2 \approx Gm_1/r$. For a 100 GeV DM particle, we find $t_{\text{relax}} \gtrsim 10^{70}$ years for the systems we consider here.

We may also worry about DM scattering with the compact object and losing energy, thereby replenishing the depleted regions of phase space. This process is only possible for DM particle moving more quickly than the orbiting object and would lead to a net ‘cooling’ for these particles [40, p. 582]. However, this process is suppressed with respect to the ‘heating’ process we have considered here by a factor m_{DM}/m_2 and can therefore be neglected. Without external perturbations, then, the disruption of the halo caused by the compact object should persist on timescales much longer than the inspiral time.

B. Spherical Symmetry

In Sec. IV, we relied on a description of the DM halo as spherically symmetric and isotropic. However, the binary is *not* spherically symmetric so we eventually expect this description to break down.

One possible issue is that the compact object scatters with particles in the DM spike only within a torus along its orbit (see Fig. 7). Thus, energy is not injected into the halo in a spherically symmetric way. Of course, particles in the DM halo are not static; particles are on orbits which are (in general) inclined with respect to the orbital plane of the binary. Thus, energy injected in the plane of the orbit will be redistributed throughout the DM halo naturally through the dynamics of the system.

More concerning is the fact that the binary will inject angular momentum into the halo, just as it injects energy. On average, the scattered particles gain angular momentum and the halo begins to co-rotate with the binary. We can estimate how rapidly the halo is spun-up by calculating the typical change in the angular momentum of a DM particle $\langle \Delta L \rangle$ each time it scatters. Comparing the torque on the compact object with the number of DM particles which scatter in a single orbit, we obtain:

$$\langle \Delta L \rangle = 4 \log \Lambda m_2 \sqrt{Gr_2} / m_1. \quad (6.2)$$

The maximum angular momentum at a given radius is achieved for circular orbits $L_{\text{max}} = \sqrt{Gm_1 r_2}$. We thus find that:

$$\frac{\langle \Delta L \rangle}{L_{\text{max}}} \approx \frac{4 \log \Lambda}{\Lambda^2} \approx 1\%, \quad (6.3)$$

for a mass ratio of $q = 10^{-3}$. Thus, the spin of the DM halo increases only by a small amount with each scatter and $\mathcal{O}(100)$ interactions are required before a particle is expected to be on a circular orbit and co-rotating with the compact object.

In a similar way, the typical change in energy of a DM particle can be calculated as:

$$\frac{\langle \Delta \mathcal{E} \rangle}{\mathcal{E}} \approx -\frac{4 \log \Lambda}{\Lambda^2} \approx -1\%, \quad (6.4)$$

where we have used the fact that the maximum energy for particles at radius r_2 is $\mathcal{E} = \sqrt{Gm_1/r_2}$. Thus, by the time a particle has scattered enough to be spun up, it will have gained enough energy to become unbound. We therefore expect that the halo will not gain a substantial net angular momentum during the inspiral.

We note also that if more DM particles *are* co-rotating, the size of the dynamical friction effect should increase. The relative velocity of encounters with the compact object will decrease, enhancing the drag force on the compact object, as described in Eq. (2.15). Thus, our approach may be seen as a conservative estimate of the size of the de-phasing effect.

Ultimately, to obtain high precision waveforms, it will be necessary to follow both the energy *and* angular momentum of DM particles in the halo. However, we expect the results we present here to be conservative, with corrections due to angular momentum injection being higher order. We defer this more detailed analysis to future work.

C. Post Newtonian corrections

We have restricted ourselves throughout this work to a Newtonian description of the binary inspiral and the DM halo. Of course, in the final stages of the inspiral, post-Newtonian corrections will become increasingly relevant and should be incorporated. A more complete description of the dynamics of the system will be developed in future work. However, we note that the dephasing signal occurs predominantly when the separation of the binary is large. At large r_2 gravitational wave losses are sub-dominant, while the orbital velocity is relatively slow, enhancing losses due to dynamical friction. While post-Newtonian corrections will of course be required for accurate waveform modelling, we do not expect them to substantially alter the de-phasing effect we study here.

DN: Should emphasize that we are just computing the dynamics of the binary in this paper in the Newtonian approximation to get an idea of the order of magnitude of the size of the effect when taking into account the feedback on the mini-halo/spike. Future work will discuss more details about the “measurability” of the dark matter effects in the gravitational waves, and treat the dynamics and waveform from the binary in more realistic ways.

BJK: David, do you have any other things you were bothered about - distortions to the halo? changing mass of the compact object?

DN: Yes, both. Also things like corrections at next order in the mass ratio. I'll fill in more details at some point.

D. Detectability

For concreteness, we have focused on the final 5 years of the inspiral, having in mind a 5-year LISA mission. Of course, there is no guarantee that the merger itself will occur during the LISA observation period. Instead, if the system is observed at an earlier time, further from inspiral, the size of the dephasing would be different. Indeed, as seen in Fig. 9, the difference in the number of cycles can be much larger if the system is detected at low frequency (or equivalently at larger orbital separation).

Ultimately, the detectability of the signal will depend on the distance to the system, the sensitivity of the proposed detector (such as LISA) and the orbital separation of the binary, as we have just discussed. In addition, in order to assess the prospects for detection, we must explore in detail how many such systems we expect to observe and with what properties. It is estimated that LISA will detect IMRIs at a rate of $\mathcal{R} \sim 3 - 10 \text{ Gpc}^{-3} \text{ yr}^{-1}$ [48]. However, only a fraction of these will be embedded in a DM spike. Very dense spikes are expected to form only at the centres of DM halos, around adiabatically growing BHs [17]. In addition, spikes may be disrupted by mergers and other dynamical processes [49].

Clearly, a more exhaustive exploration of the parameter space is warranted, taking into account the population properties of IMRI systems, in order to assess detectability of the inspiral signal and associated dephasing. These topics will be addressed in follow-up work.

VII. CONCLUSIONS

Dark Matter overdensities around intermediate mass black holes inevitably modify the dynamics of inspiraling compact objects, and could potentially be detected through their impact on the gravitational waveform produced by the binary inspiral.

We have demonstrated that previous analyses have largely overestimated the dephasing induced by the dynamical friction experienced by the compact object ploughing through the dense dark matter spike. Those studies relied in fact on the simplifying assumption of a ‘static’ dark matter distribution, whereas we have shown here that there is an efficient transfer of energy from the binary to the dark matter spike. The energy dissipated by dynamical friction can in fact be much larger than the binding energy in the DM distribution.

We have then introduced a prescription to update the

dark matter phase space density as the binary evolves. Dynamical friction in general speeds up the inspiral, reducing the number of GW cycles which would be observed by experiments such as LISA. Compared to the case of a static spike, our prescription leads to a depletion of the DM density at the orbital radius, which in turn reduces the size of the dynamical friction force and thus slows the inspiral. This has dramatic consequences for the detectability of the GW dephasing, and its interpretation.

For a central IMBH with $m_1 = 10^3 M_\odot$, assuming a static DM spike with slope $\gamma = 7/3$, leads to a 20% difference in the number of cycles with respect to the vacuum case. When the dynamical evolution of the spike is taken into account according to our prescription, we find that the difference is reduced by a factor of ~ 100 , to 0.2%. The effect tends to be smaller for higher mass ratios. For a heavier central IMBH of $m_2 = 10^4 M_\odot$, our prescription leads only to a 60% difference in dephasing, with respect to the static case. That however corresponds to 29000 GW cycles, which should be observable and distinguishable by LISA.

Dynamical friction significantly shortens the inspiral time. For a mass ratio $q = 10^3$, a 5-year inspiral in vacuum would be shortened by more than 1 year in the presence of a static DM spike with $\gamma = 7/3$. We have however shown that incorporating the feedback on the dark matter distribution leads to a difference in inspiral time with respect to the vacuum case of only 12 days. We also found that the dephasing effect is very sensitive to the slope of the DM distribution, rapidly becoming undetectable for a mild slope of $\gamma = 3/2$.

Outlook.. [say we postpone forecasts / reconstruction of spike parameters / nature of dark matter to future work]

ACKNOWLEDGMENTS

The authors would like to thank Jonathan Baird, Priscilla Canizares, Adam Coogan, Tom Edwards, Tanja Hinderer and Samaya Nissanke for helpful discussions about this work. B.J.K. also thank Rebekka Bieri and Jonathan Coles for useful guidance about N -body simulations.

D.A.N. acknowledges the support of the Netherlands Organization for Scientific Research through the NWO VIDI Grant No. 639.042.612-Nissanke. DG has received financial support through the Postdoctoral Junior Leader Fellowship Programme from la Caixa Banking Foundation (grant n. LCF/BQ/LI18/11630014). DG was also supported by the Spanish Agencia Estatal de Investigación through the grants PGC2018-095161-B-I00, IFT Centro de Excelencia Severo Ochoa SEV-2016-0597, and Red Consolider MultiDark FPA2017-90566-REDC.

This work was carried out on the Dutch national e-infrastructure with the support of SURF Cooperative. Finally, we acknowledge the use of the Python scientific computing packages NumPy [50] and SciPy [51].

-
- [1] B. P. Abbott *et al.* (LIGO Scientific, Virgo), “Observation of Gravitational Waves from a Binary Black Hole Merger,” *Phys. Rev. Lett.* **116**, 061102 (2016), [arXiv:1602.03837 \[gr-qc\]](#).
- [2] B. P. Abbott *et al.* (LIGO Scientific, Virgo), “GW170817: Observation of Gravitational Waves from a Binary Neutron Star Inspiral,” *Phys. Rev. Lett.* **119**, 161101 (2017), [arXiv:1710.05832 \[gr-qc\]](#).
- [3] B. P. Abbott *et al.* (LIGO Scientific, Virgo, Fermi GBM, INTEGRAL, IceCube, AstroSat Cadmium Zinc Telluride Imager Team, IPN, Insight-Hxmt, ANTARES, Swift, AGILE Team, 1M2H Team, Dark Energy Camera GW-EM, DES, DLT40, GRAWITA, Fermi-LAT, ATCA, ASKAP, Las Cumbres Observatory Group, OzGrav, DWF (Deeper Wider Faster Program), AST3, CAAS-TRO, VINROUGE, MASTER, J-GEM, GROWTH, JAGWAR, CaltechNRAO, TTU-NRAO, NuSTAR, Pan-STARRS, MAXI Team, TZAC Consortium, KU, Nordic Optical Telescope, ePESSTO, GROND, Texas Tech University, SALT Group, TOROS, BOOTES, MWA, CALET, IKI-GW Follow-up, H.E.S.S., LOFAR, LWA, HAWC, Pierre Auger, ALMA, Euro VLBI Team, Pi of Sky, Chandra Team at McGill University, DFN, ATLAS Telescopes, High Time Resolution Universe Survey, RIMAS, RATIR, SKA South Africa/MeerKAT), “Multi-messenger Observations of a Binary Neutron Star Merger,” *Astrophys. J.* **848**, L12 (2017), [arXiv:1710.05833 \[astro-ph.HE\]](#).
- [4] B. P. Abbott *et al.* (LIGO Scientific, Virgo), “GWTC-1: A Gravitational-Wave Transient Catalog of Compact Binary Mergers Observed by LIGO and Virgo during the First and Second Observing Runs,” (2018), [arXiv:1811.12907 \[astro-ph.HE\]](#).
- [5] David Shoemaker (LIGO Scientific), “Gravitational wave astronomy with LIGO and similar detectors in the next decade,” (2019), [arXiv:1904.03187 \[gr-qc\]](#).
- [6] T. Akutsu *et al.* (KAGRA), “First cryogenic test operation of underground km-scale gravitational-wave observatory KAGRA,” *Class. Quant. Grav.* **36**, 165008 (2019), [arXiv:1901.03569 \[astro-ph.IM\]](#).
- [7] Pau Amaro-Seoane *et al.*, “eLISA/NGO: Astrophysics and cosmology in the gravitational-wave millihertz regime,” *GW Notes* **6**, 4–110 (2013), [arXiv:1201.3621 \[astro-ph.CO\]](#).
- [8] Pau Amaro-Seoane *et al.*, “Laser Interferometer Space Antenna,” (2017), [arXiv:1702.00786 \[astro-ph.IM\]](#).
- [9] B. Sathyaprakash *et al.*, “Scientific Objectives of Einstein Telescope,” *Gravitational waves. Numerical relativity - data analysis. Proceedings, 9th Edoardo Amaldi Conference, Amaldi 9, and meeting, NRDA 2011, Cardiff, UK, July 10-15, 2011*, *Class. Quant. Grav.* **29**, 124013 (2012), [Erratum: *Class. Quant. Grav.* **30**, 079501 (2013)], [arXiv:1206.0331 \[gr-qc\]](#).
- [10] G. Hobbs, A. Archibald, Z. Arzoumanian, D. Backer, M. Bailes, N. D. R. Bhat, M. Burgay, S. Burke-Spolaor, D. Champion, and I. Cognard, “The International Pulsar Timing Array project: using pulsars as a gravitational wave detector,” *Classical and Quantum Gravity* **27**, 084013 (2010), [arXiv:0911.5206 \[astro-ph.SR\]](#).
- [11] M. Kramer and D. J. Champion, “The European Pulsar Timing Array and the Large European Array for Pulsars,” *Classical and Quantum Gravity* **30**, 224009 (2013).
- [12] Leor Barack *et al.*, “Black holes, gravitational waves and fundamental physics: a roadmap,” *Class. Quant. Grav.* **36**, 143001 (2019), [arXiv:1806.05195 \[gr-qc\]](#).
- [13] Gianfranco Bertone and M. P. Tait, Tim, “A new era in the search for dark matter,” *Nature* **562**, 51–56 (2018), [arXiv:1810.01668 \[astro-ph.CO\]](#).
- [14] Gianfranco Bertone *et al.*, “Gravitational wave probes of dark matter: challenges and opportunities,” (2019), [arXiv:1907.10610 \[astro-ph.CO\]](#).
- [15] Gerald D. Quinlan, Lars Hernquist, and Stein Sigurdsson, “Models of Galaxies with Central Black Holes: Adiabatic Growth in Spherical Galaxies,” *Astrophys. J.* **440**, 554–564 (1995), [arXiv:astro-ph/9407005 \[astro-ph\]](#).
- [16] Paolo Gondolo and Joseph Silk, “Dark matter annihilation at the galactic center,” *Phys. Rev. Lett.* **83**, 1719–1722 (1999), [arXiv:astro-ph/9906391 \[astro-ph\]](#).
- [17] Piero Ullio, HongSheng Zhao, and Marc Kamionkowski, “A Dark matter spike at the galactic center?” *Phys. Rev. D* **64**, 043504 (2001), [arXiv:astro-ph/0101481 \[astro-ph\]](#).
- [18] Gianfranco Bertone and David Merritt, “Time-dependent models for dark matter at the Galactic Center,” *Phys. Rev. D* **72**, 103502 (2005), [arXiv:astro-ph/0501555 \[astro-ph\]](#).
- [19] Kazunori Kohri, Tomohiro Nakama, and Teruaki Suyama, “Testing scenarios of primordial black holes being the seeds of supermassive black holes by ultracompact minihalos and CMB μ -distortions,” *Phys. Rev. D* **90**, 083514 (2014), [arXiv:1405.5999 \[astro-ph.CO\]](#).
- [20] Yu. N. Eroshenko, “Dark matter density spikes around primordial black holes,” *Astron. Lett.* **42**, 347–356 (2016), [*Pisma Astron. Zh.* **42**, no. 6, 359 (2016)], [arXiv:1607.00612 \[astro-ph.HE\]](#).
- [21] Sofiane M. Boucenna, Florian Kuhnel, Tommy Ohlsson, and Luca Visinelli, “Novel Constraints on Mixed Dark-Matter Scenarios of Primordial Black Holes and WIMPs,” *JCAP* **1807**, 003 (2018), [arXiv:1712.06383 \[hep-ph\]](#).
- [22] Kazunari Eda, Yousuke Itoh, Sachiko Kuroyanagi, and Joseph Silk, “New Probe of Dark-Matter Properties: Gravitational Waves from an Intermediate-Mass Black Hole Embedded in a Dark-Matter Minispike,” *Phys. Rev. Lett.* **110**, 221101 (2013), [arXiv:1301.5971 \[gr-qc\]](#).
- [23] Kazunari Eda, Yousuke Itoh, Sachiko Kuroyanagi, and Joseph Silk, “Gravitational waves as a probe of dark matter minispikes,” *Phys. Rev. D* **91**, 044045 (2015), [arXiv:1408.3534 \[gr-qc\]](#).
- [24] Caio F. B. Macedo, Paolo Pani, Vitor Cardoso, and Lus C. B. Crispino, “Into the lair: gravitational-wave signatures of dark matter,” *Astrophys. J.* **774**, 48 (2013), [arXiv:1302.2646 \[gr-qc\]](#).
- [25] Enrico Barausse, Vitor Cardoso, and Paolo Pani, “Can environmental effects spoil precision gravitational-wave astrophysics?” *Phys. Rev. D* **89**, 104059 (2014), [arXiv:1404.7149 \[gr-qc\]](#).
- [26] Enrico Barausse, Vitor Cardoso, and Paolo Pani, “Environmental Effects for Gravitational-wave Astrophysics,” *Proceedings, 10th International LISA Symposium: Gainesville, Florida, USA, May 18-23, 2014*, *J. Phys. Conf. Ser.* **610**, 012044 (2015), [arXiv:1404.7140 \[astro-ph.CO\]](#).

- [27] Xiao-Jun Yue and Wen-Biao Han, “Gravitational waves with dark matter minispikes: the combined effect,” *Phys. Rev. D* **97**, 064003 (2018), [arXiv:1711.09706 \[gr-qc\]](#).
- [28] Xiao-Jun Yue, Wen-Biao Han, and Xian Chen, “Dark matter: an efficient catalyst for intermediate-mass-ratio-inspiral events,” *Astrophys. J.* **874**, 34 (2019), [arXiv:1802.03739 \[gr-qc\]](#).
- [29] Otto A. Hannuksela, Kenny C. Y. Ng, and Tjonnie G. F. Li, “Extreme Dark Matter Tests with Extreme Mass Ratio Inspirals,” (2019), [arXiv:1906.11845 \[astro-ph.CO\]](#).
- [30] Vitor Cardoso and Andrea Maselli, “Constraints on the astrophysical environment of binaries with gravitational-wave observations,” (2019), [arXiv:1909.05870 \[astro-ph.HE\]](#).
- [31] S. Chandrasekhar, “Dynamical friction. i. general considerations: the coefficient of dynamical friction.” *The Astrophysical Journal* **97**, 255 (1943).
- [32] S. Chandrasekhar, “Dynamical friction. II. the rate of escape of stars from clusters and the evidence for the operation of dynamical friction.” *The Astrophysical Journal* **97**, 263 (1943).
- [33] S. Chandrasekhar, “Dynamical friction. III. a more exact theory of the rate of escape of stars from clusters.” *The Astrophysical Journal* **98**, 54 (1943).
- [34] Keith A. Arnaud *et al.*, “The Mock LISA Data Challenges: An overview,” *Proceedings, 6th International LISA Symposium on Laser interferometer space antenna: Greenbelt, USA, June 19-23, 2006, AIP Conf. Proc.* **873**, 619–624 (2006), [arXiv:gr-qc/0609105 \[gr-qc\]](#).
- [35] Stanislav Babak *et al.* (Mock LISA Data Challenge Task Force), “The Mock LISA Data Challenges: From Challenge 3 to Challenge 4,” *Gravitational waves. Proceedings, 8th Edoardo Amaldi Conference, Amaldi 8, New York, USA, June 22-26, 2009, Class. Quant. Grav.* **27**, 084009 (2010), [arXiv:0912.0548 \[gr-qc\]](#).
- [36] “Lisa data challenges,” <https://lisa-ldc.lal.in2p3.fr/>.
- [37] Laleh Sadeghian, Francesc Ferrer, and Clifford M. Will, “Dark matter distributions around massive black holes: A general relativistic analysis,” *Phys. Rev. D* **88**, 063522 (2013), [arXiv:1305.2619 \[astro-ph.GA\]](#).
- [38] Francesc Ferrer, Augusto Medeiros da Rosa, and Clifford M. Will, “Dark matter spikes in the vicinity of Kerr black holes,” *Phys. Rev. D* **96**, 083014 (2017), [arXiv:1707.06302 \[astro-ph.CO\]](#).
- [39] Zhaoyi Xu, Xiaobo Gong, and Shuang-Nan Zhang, “Black hole immersed dark matter halo,” *Phys. Rev. D* **101**, 024029 (2020).
- [40] J. Binney and S. Tremaine, *Galactic Dynamics: Second Edition*, by James Binney and Scott Tremaine. ISBN 978-0-691-13026-2 (HB). Published by Princeton University Press, Princeton, NJ USA, 2008. (Princeton University Press, 2008).
- [41] Feryal zel and Paulo Freire, “Masses, Radii, and the Equation of State of Neutron Stars,” *Ann. Rev. Astron. Astrophys.* **54**, 401–440 (2016), [arXiv:1603.02698 \[astro-ph.HE\]](#).
- [42] Volker Springel, Naoki Yoshida, and Simon D. M. White, “GADGET: A Code for collisionless and gasdynamical cosmological simulations,” *New Astron.* **6**, 79 (2001), [arXiv:astro-ph/0003162 \[astro-ph\]](#).
- [43] Volker Springel, “The Cosmological simulation code GADGET-2,” *Mon. Not. Roy. Astron. Soc.* **364**, 1105–1134 (2005), [arXiv:astro-ph/0505010 \[astro-ph\]](#).
- [44] Thomas D. P. Edwards, Marco Chianese, Bradley J. Kavanagh, Samaya M. Nissanke, and Christoph Weniger, “A Unique Multi-Messenger Signal of QCD Axion Dark Matter,” (2019), [arXiv:1905.04686 \[hep-ph\]](#).
- [45] David Merritt, Stefan Harfst, and Gianfranco Bertone, “Collisionally Regenerated Dark Matter Structures in Galactic Nuclei,” *Phys. Rev. D* **75**, 043517 (2007), [arXiv:astro-ph/0610425 \[astro-ph\]](#).
- [46] J. N. Bahcall and R. A. Wolf, “Star distribution around a massive black hole in a globular cluster,” *Astrophys. J.* **209**, 214–232 (1976).
- [47] A. P. Lightman and S. L. Shapiro, “The distribution and consumption rate of stars around a massive, collapsed object,” *Astrophys. J.* **211**, 244–262 (1977).
- [48] Giacomo Fragione, Idan Ginsburg, and Bence Kocsis, “Gravitational Waves and Intermediate-mass Black Hole Retention in Globular Clusters,” *Astrophys. J.* **856**, 92 (2018), [arXiv:1711.00483 \[astro-ph.GA\]](#).
- [49] Mark Wanders, Gianfranco Bertone, Marta Volonteri, and Christoph Weniger, “No WIMP Mini-Spikes in Dwarf Spheroidal Galaxies,” *JCAP* **1504**, 004 (2015), [arXiv:1409.5797 \[astro-ph.HE\]](#).
- [50] Travis Oliphant, “NumPy: A guide to NumPy,” USA: Trelgol Publishing (2006–), [Online; accessed 08/05/2019].
- [51] Eric Jones, Travis Oliphant, Pearu Peterson, *et al.*, “SciPy: Open source scientific tools for Python,” (2001–), [Online; accessed 08/05/2019].
- [52] Long Do Cao, “pygadgetic,” <https://github.com/ldocao/pygadgetic> (2015).
- [53] R. Thompson, “pyGadgetReader: GADGET snapshot reader for python,” Astrophysics Source Code Library (2014), [ascl:1411.001](#).
- [54] The NIST Reference on Constants, Units, and Uncertainty, “2018 CODATA Value: Newtonian constant of gravitation,” <https://physics.nist.gov/cgi-bin/cuu/Value?bg> (2018).
- [55] DLMF, “NIST Digital Library of Mathematical Functions,” <http://dlmf.nist.gov/>, Release 1.0.25 of 2019-12-15, f. W. J. Olver, A. B. Olde Daalhuis, D. W. Lozier, B. I. Schneider, R. F. Boisvert, C. W. Clark, B. R. Miller, B. V. Saunders, H. S. Cohl, and M. A. McClain, eds.

Appendix A: An effective model based on ejecting spherical shells of dark matter

In this subsection, we define a prescription to evolve a compact binary with DM between separations r_i and r_f such that the total energy input into the DM distribution is equal to the binding energy of the spherical shell of DM between r_i and r_f . We implement this procedure as follows. Instead of equating the rate of energy dissipation by GWs in Eq. (2.14) to be equal to minus the rate of change of the orbital energy, we set the GW dissipation equal to the orbital energy minus the energy of a shell of DM of width dr_2 at the boisus r_2 of the circular orbit. Thus, we write

$$\frac{dE_{\text{GW}}}{dt} = \frac{dr_2}{dt} \left(\frac{dE_{\text{orbit}}}{dr_2} - \frac{dU_{\text{sh}}}{dr_2} \right). \quad (\text{A1})$$

In Eq. (A1) the three derivatives of energies that ap-

pear can be obtained from Eqs. (2.8), (2.12), and (2.14), thereby leaving dr_2/dt as the one unknown quantity. We can then use Eq. (A1) to compute the time for the binary to inspiral between radii r_i and r_f . We write the result as

$$\Delta t = \left(\frac{5c^5(r_2)^4}{256G^3Mm_1m_2} \right) \times \left\{ 1 - \frac{(3 - \gamma_{\text{sp}})m_{\text{DM}}(r_2)}{m_1m_2} \left[\frac{2(m_1 - m_{\text{in}})}{7 - \gamma_{\text{sp}}} + \frac{m_{\text{DM}}(r_2)}{5 - \gamma_{\text{sp}}} \right] \right\} \Big|_{r_f}^{r_i}. \quad (\text{A2})$$

The first line of Eq. (A2) is the usual leading PN order expression for the time elapsed between two circular radii. The second line of this equation is a decrease in this time that arises, because, in this effective model, passing through each shell of DM of radius r and thickness dr takes away a fraction of the available orbital energy that would otherwise be lost to GW dissipation.

Because we are typically interested in the last few years of the inspiral before merger, the DM contained within r_1 is generally small. This means that the term in square brackets in Eq. (A2) will just go as $2m_1/(7 - \gamma_{\text{sp}})$; thus the difference of the time elapsed between two radii from that without dark matter will be proportional to $m_{\text{DM}}(r_i)/m_2$. For example in the fiducial case in Eda *et al.*, this number is around $m_{\text{DM}}(r_i)/m_2 \sim 0.005$. Over five years of inspiraling, this will lead to at least 10^4 fewer orbits (given that the initial orbital period is around 100 s). Thus, in this model based on not dissipating more energy than the gravitational binding energy of DM shells at this radius, there is sufficient energy in the DM spike to have a large impact on the inspiral of the small compact object into the IMBH.

Note, however, that simply having sufficient binding energy in the dark matter distribution around the black hole does not mean that the entirety of this potential energy can be dissipated through the scatterings that induce dynamical friction on the small compact object. Instead it should be thought of as a more conservative, though still rough, upper limit on the size of the effect that is likely to occur. A more precise estimate of the effect will be based on the prescription described in Sec. IV and will be given in Sec. V.

DN: May include more numbers or visuals if useful...

Appendix B: N -body simulations

Here, we provide more technical details about the N -body simulations described in Sec. III. We use the publicly available GADGET-2 code [42, 43], with minor modification which we describe below. In order to specify initial conditions and read the GADGET snapshots in Python, we use PYGADGETIC [52] and PYGADGETREADER [53].

ErrTolForceAcc	10^{-5}		
ErrTolIntAccuracy	10^{-3}		
MaxTimestep (BH) [s]	1.5×10^{-3}		
MaxTimestep (DM) [s]	1.5×10^3		
$m_1 =$	$100 M_\odot$	$300 M_\odot$	$1000 M_\odot$
ℓ_{soft} [pc]	10^{-10}	10^{-10}	2.4×10^{-11}

TABLE III. **Summary of Gadget-2 parameters.** The parameter **ErrTolForceAcc** controls the accuracy of force calculations, while **ErrTolIntAccuracy** determines the error in the time integration. We specify the softening lengths ℓ_{soft} , for which we use a slightly smaller value for simulations with m_1 . Each simulation contains $2^{15} \approx 33000$ DM particles.

We fix the softening length to be $\ell_{\text{soft}} \approx 10^{-10}$ pc, approximately the Schwarzschild radius for a $1000 M_\odot$ black hole. For the simulations using a central mass of $1000 M_\odot$, we reduce the softening length by roughly a factor of 4. This enhances our sensitivity to the small dynamical friction effect, as described in the main text. We have modified GADGET-2 to allow for a different maximum timestep for the DM particles and the compact objects. We set the maximum timestep for DM particles to be comparable to the typical orbital period $\mathcal{O}(1000 \text{ s})$, while the timestep for the orbiting compact objects is set a factor of 10^{-6} smaller. This allows us to trace the binary separation with sufficient precision (as illustrated in Fig. 4). A summary of the parameters used in the simulations is given in Tab. III.

Our only other modification of GADGET-2 is to alter the hard-coded value of Newton's constant G . The release version of GADGET-2 uses a value $G = 6.672 \times 10^{-11} \text{ m}^3 \text{ kg}^{-1} \text{ s}^{-2}$. This value of a factor of $\sim 3 \times 10^{-4}$ smaller than the current recommended value for G_N [54]. This discrepancy is comparable to the relative change in orbital radius which we are hoping to observe (see Fig. 4). Thus, it was necessary to change the hard-coded value to match the current value used elsewhere in our analysis chain.

For the purposes of the simulations, we model the DM spike using a generalised NFW profile:

$$\rho_{\text{DM}} = \frac{\rho_{\text{sp}}}{(r/r_{\text{sp}})^\gamma (1 + r/r_t)^\alpha}. \quad (\text{B1})$$

We set $\alpha = 2$, so that the profile drops off rapidly above the truncation radius r_t . This produces an equilibrium configuration with the correct density profile in the inner region of interest (to within a few percent) while keeping the total mass of the spike computationally feasible. We set the truncation radius equal to

$$r_t = 10^{-5} r_{\text{sp}} \left(\frac{100 M_\odot}{m_1} \right)^{3/2}, \quad (\text{B2})$$

which means that the total mass of the simulated spike is approximately the same for the different values of m_1 we consider. We use $N = 2^{15}$ DM particles in each simulation and have checked that the spike profile is stable on the timescales of our simulations.

Each binary is initialized on a circular orbit around the barycentre of the system. We follow separation of the two compact objects as a function of time to directly measure the dynamical friction force. We perform simulations with at least 5 different random realisations of the DM spike in order to extract an estimate of the error. The results are reported in Figs. 5 and 6.

Appendix C: Scattering probability

We wish to evaluate the probability that a particle with energy \mathcal{E} scatters to an energy $\mathcal{E} + \Delta\mathcal{E}$. This is given in Eq. (4.15), which we repeat here:

$$P_s(\mathcal{E}, \Delta\mathcal{E}) = \frac{4\pi^2 r_2 b_{90}^2}{g(\mathcal{E}) v_0^2} \left[1 + \frac{b_\star^2}{b_{90}^2} \right]^2 \times \int \sqrt{2(\Psi(r[b_\star, \alpha]) - \mathcal{E})} \sin(\theta[b_\star, \alpha]) d\alpha. \quad (\text{C1})$$

We recall that $b_\star = b_\star(\Delta\mathcal{E})$ and that the integration is over values of $\alpha \in [0, \pi]$ such that $r[b_\star, \alpha] \in [r_{\text{cut}}, r_{\mathcal{E}}]$. It is useful to recall also that $\Psi(r) = Gm_1/r$ and

$$r = \sqrt{r_2^2 + b_\star^2 + 2r_2 b_\star \cos \alpha}, \quad (\text{C2})$$

$$\sin \theta = \frac{r_2 + b_\star \cos \alpha}{\sqrt{r_2^2 + b_\star^2 + 2r_2 b_\star \cos \alpha}}.$$

Expanding to first order in (b/r_2) , we obtain:

$$r \approx r_2 + b_\star \cos \alpha + \mathcal{O}(b_\star^2) \quad (\text{C3})$$

$$\approx \frac{r_2}{1 - (b_\star/r_2) \cos \alpha}.$$

This in turn gives:

$$\sin \theta \approx 1 + \mathcal{O}(b_\star^2), \quad (\text{C4})$$

$$\Psi(r) \approx \Psi(r_2) (1 - (b_\star/r_2) \cos \alpha + \mathcal{O}(b_\star^2)).$$

The integral over the angle α can then be written:

$$\int_{\alpha_1}^{\alpha_2} \sqrt{2(\Psi(r) - \mathcal{E})} d\alpha = 2\sqrt{2\Psi(r_2)} \sqrt{1 - \frac{r_2}{r_{\mathcal{E}}} + \frac{b_\star}{r_2}} \times \left[E\left(\frac{\pi - \alpha_1}{2}, m\right) - E\left(\frac{\pi - \alpha_2}{2}, m\right) \right], \quad (\text{C5})$$

where $E(\varphi, m)$ is the incomplete elliptic integral of the second kind:

$$E(\varphi, m) = \int_0^\varphi \sqrt{1 - m \sin^2 \theta} d\theta, \quad (\text{C6})$$

and

$$m = \frac{2(b_\star/r_2)}{1 - \frac{r_2}{r_{\mathcal{E}}} + \frac{b_\star}{r_2}}. \quad (\text{C7})$$

The limits of integration are set by requiring $r \in [r_{\text{cut}}, r_{\mathcal{E}}]$ which gives, again to first order in (b/r_\star) :

$$\alpha_1 = \cos^{-1} \left\{ \min \left((r_2 - r_2^2/r_{\mathcal{E}})/b_\star, 1 \right) \right\}, \quad (\text{C8})$$

$$\alpha_2 = \cos^{-1} \left\{ \max \left((r_2 - r_2^2/r_{\text{cut}})/b_\star, -1 \right) \right\}.$$

The scattering probability $P_s(\mathcal{E}, \Delta\mathcal{E})$ can now be evaluated in terms of special functions.⁴ With this, there is only a single numerical integral (over $\Delta\mathcal{E}$) to be performed to evaluate df/dt in Eq. (4.7).

⁴ On a technical note, the SciPy implementation of $E(\varphi, m)$ is valid only for $m \leq 1$. To extend to values of $m > 1$, it is necessary to

perform reciprocal modulus transformations; see Eq. (19.7.4) in Ref. [55].